

Gas Generation Potential and Characteristics of Oil-Prone Shale in the Saline Lacustrine Rifting Basins: A Case Study of the Dongpu Depression, Bohai Bay Basin

Pengyuan Zhang, Fujie Jiang,* Chenxi Zhu, Renda Huang, Tao Hu, Tianwu Xu, Wendu Li, and Hang Xiong

Cite This: *Energy Fuels* 2021, 35, 2192–2208

Read Online

ACCESS |

Metrics & More

Article Recommendations

ABSTRACT: In comparison to the continuous breakthrough in shale gas of marine basins, the pace of study of lacustrine basins is relatively slow. The latest studies have shown the saline lacustrine rifting basins (SLRBs) are one of the favorable exploration areas from the view of shale pore, mineral composition, and organic matter accumulation. However, the study on the gas generation potential and characteristics is still lacking because the traditional view is that lacustrine source rocks are oil-prone. Therefore, to identify gas generation potential and characteristics of oil-prone shale in SLRBs, the samples from the saline area (SA) and non-saline area (NA) of the Dongpu Depression are selected for the organic geochemical experiments and closed gold cube thermal simulation experiments. Geochemical results show that the SA samples are definitely oil-prone source rocks with high quality, and their main type is II kerogen. However, the results from thermal simulation experiments indicate that the gas generation potential of oil-prone shale in SLRBs is enough for the accumulation of shale gas with the peak gas yield of 469.11 mg/g of TOC at the heating rate of 20 °C/h TOC and 466.75 mg/g of TOC at the heating rate of 2 °C/h and TOC. Moreover, according to the dynamic hydrocarbon yields and carbon isotope ($\ln C_2/C_3$, $\ln C_1/C_2$, and $\delta^{13}C_1-\delta^{13}C_2$) during the increasing temperature, the gas generation process for SA and NA samples can be divided into three stages: kerogen cracking, oil cracking, and wet gas cracking. In comparison to other types of source rocks (marine shale, coal, and coal mudstone), the SA oil-prone shale can experience longer intervals in kerogen cracking and oil cracking, which may be the main stage of gas generation. The model based on kinetic parameters shows that the main gas generation period for SA and NA samples is the late Es₁ (the first member of Shahejie Formation) to Ed (the Dongying Formation) of the Early Cenozoic, which can be consist of the depression stage with the deepest depth and the largest subsidence amplitude in the Dongpu Depression. Such information can be a reference for other SLRBs.

1. INTRODUCTION

Oil and gas are the daily necessities of people and important strategic resources in modern society.¹ The concept of “continuous-type petroleum accumulation” proposed by Schmoker,² which has become a cutting-edge topic of unconventional petroleum geology, is a significant milestone in petroleum geology. More than 20 years after that, shale resources, tight gas, coalbed gas, tar sands, etc. have gradually become the focus of petroleum geology.^{3–8} In addition, in comparison to other types of unconventional energy, shale gas has two advantages: (1) low carbon dioxide emission⁹ and (2) zero sulfur dioxide content.¹⁰ Therefore, traditional fossil fuels, which are not environmentally friendly, may still dominate in the energy structure in the near future but will account for a smaller and smaller share, and gas will account for a larger share.^{11–14}

In comparison to the constant breakthroughs of shale gas in the marine basins globally, including Northern American Haynesville shale,^{15,16} Canadian Montney shale,¹⁷ and South-eastern China Ordovician–Silurian shale,¹⁸ the pace of exploration in lacustrine basins is relatively slow. Oil-prone source rocks are the main source rocks in lacustrine basins, which leads to the relatively lack of studies on lacustrine shale

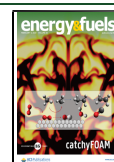
gas. However, according to the hydrocarbon generation model of source rocks in the classical petroleum geology theory, the oil generation is always accompanied by gas.¹⁹ Furthermore, the recent discovery of the Bozhong 19-6 gas field (situated in Bozhong Depression, Bohai Bay Basin) also proves that there is great potential for natural gas exploration.²⁰

According to Mello and Karner,²¹ 33% of the 334 large oil and gas fields in the world have developed salt rocks and gypsum rocks. In some counties, such as China and Brazil, the total petroleum and natural gas resources are dominated by those from lacustrine basins. Furthermore, source rocks with high organic matter (OM), which are the base of shale oil and gas resources, are always associated with salt rocks and gypsum–salt rocks.²² Therefore, the saline lacustrine rifting basins (SLRBs) are receiving more and more attention among

Received: November 24, 2020

Revised: January 3, 2021

Published: January 15, 2021



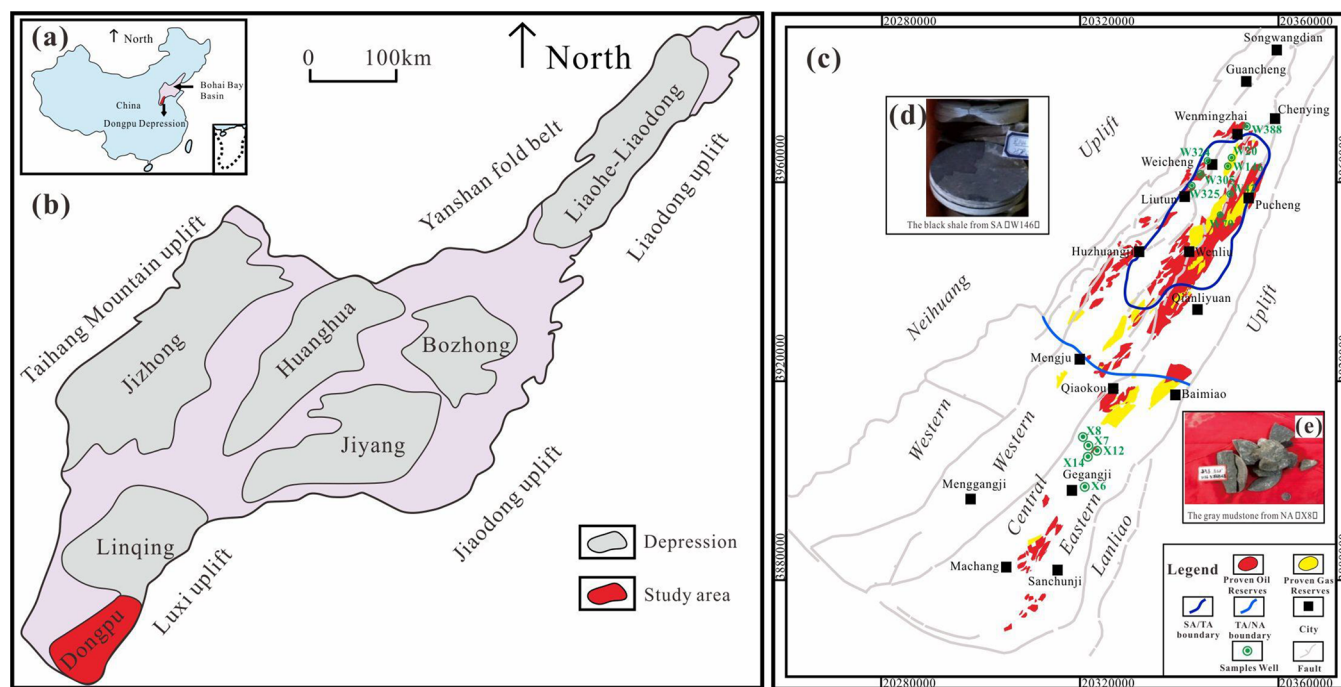


Figure 1. Geological setting of the Dongpu Depression, Bohai Bay Basin: (a) location map of the Bohai Bay Basin, (b) location map of the Dongpu Depression, (c) regional geologic maps of the Dongpu Depression showing the distribution of the proven hydrocarbon reserves, main faults, and tectonic zones, and (e) photo of NA mudstone. SA and NA represent the saline area and non-saline area of the Dongpu Depression.

various lacustrine basins as a result of the excellent potential of hydrocarbon resources. Recently, massive studies on the shale resources in SLRBs continue to be published, mainly focusing on shale geological and geochemical characteristics,^{23–25} shale pore structure,^{25,26} OM enrichment in shale,²⁷ shale storage capacity,²⁸ and strong heterogeneity,²⁷ which further exhibit the great potential of source rocks in SLRBs. However, the studies on the quantification of gas generation potential and the gas generation process for those oil-prone source rocks in SLRBs, which are the supporting foundation of shale gas reservoir potential, are still lacking.

According to that above, the gas generation capacity of the oil-prone shale in SLRBs needs to be deeply studied. A short-time and high-temperature thermal simulation experiment can effectively simulate the evolution process and capacity of source rocks in the scale of geologic historical periods. Thermal simulation of kerogen can also detect the gas product yield and stable carbon isotope composition.^{29–32} The anhydrous open system, hydrous closed system, and anhydrous closed system are three main types of thermal simulation experiments.^{33,34} As a result of the poor hydrocarbon expulsion effect caused by the densification of the shale, the closed thermal simulation system is adopted in this research. Additionally, because of the high melting point of gold, gold cubes can be used as containers to simulate the effect of a high temperature on the thermal evolution of OM.³⁵ Finally, the anhydrous closed gold tube thermal simulation experiments are carried out in this study.

Bohai Bay Basin (BBB) is an important petroliferous lacustrine basin in eastern China,³⁶ and this basin can be divided into 50 depressions³⁷ (Figure 1). The Dongpu Depression is a typical SLRB in China, with three dominant kinds of depositional environments on the plane (saline, brackish, and non-saline) in the Paleogene²⁷ (Figure 1). Previous studies on the Dongpu Depression have shown that the source rocks in saline and brackish environments are the

main hydrocarbons generation rocks, and the paleo-salinity is one of the controlling factors for the enrichment of OM.^{27,38} Hence, the shale in saline environments is a suitable candidate sample for closed gold cube thermal simulation experiments in this study. To highlight the gas hydrocarbon generation characteristics of the shale in the saline area (SA), a mudstone sample in the non-saline area (NA) was selected as the control sample.

Therefore, through geochemical experiments and closed gold tube thermal simulation experiments, the purpose of this study is to (1) evaluate the gas generation potential of SA shale in SLRBs in contrast to that of NA mudstone, (2) explore the gas generation characteristics (process) of SA shale in SLRBs, and (3) simulate the total hydrocarbon gas generation history of the SA shale and NA mudstone based on kinetic parameters derived from the confined pyrolysis experiments. Such information can not only provide a theoretical basis for gas exploration in the Dongpu Depression but also be a reference for other SLRBs.

2. GEOLOGICAL BACKGROUND

The Dongpu Depression is located in the southern part of BBB, and the east and west sides are held by the Luxi uplift and Neihuang uplift, with a shape of “long in the north–south and narrow in the east–west”³⁹ (Figure 1). This depression is a Cenozoic rifting sag developed in the North China Plate and can be divided into five main parts: Lanliao fault zone, eastern depression zone, central uplift zone, western depression zone, and western slope zone.⁴⁰ The Dongpu Depression experienced the faulting stage in the Paleogene and the depression stage in the Neogene–Quaternary in geological history, and it is generally characterized by the construction of “rifting in the east and overlapping in the west; sloping to the east”⁴¹ (Figure 1). Previous studies show that the Dongpu Depression belongs to the Linqing Sub-basin. However, recent studies illustrate

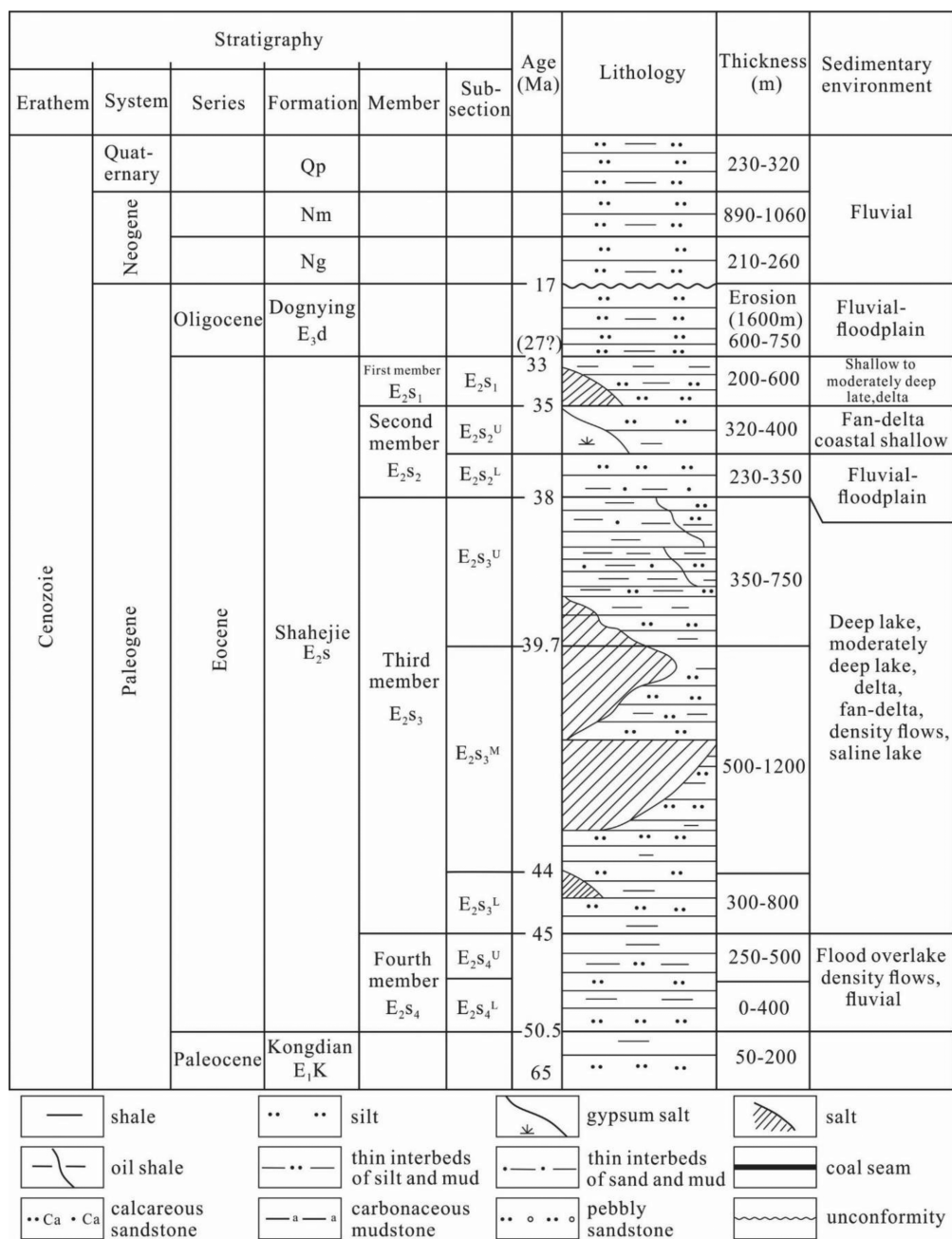


Figure 2. Stratigraphic column of the Palaeogene in the Dongpu Depression.

that the geological structure, sedimentation, and tectonic evolution of the Dongpu Depression are quite different from other depressions in the Linqing Sub-basin, which indicates that the Dongpu Depression should be an independent tectonic unit in BBB.⁴²

In the early Cenozoic Himalayan movement, under the double influence of Pacific plate subduction and Indian Ocean plate compression, the Dongpu Depression entered the stage of faulting, and the fourth member of Shahejie Formation (Es₄) and the third member of Shahejie Formation (Es₃) deposited and then entered the stage of transformation from fault depression to depression, and the second member of Shahejie Formation (Es₂) and the first member of Shahejie Formation (Es₁) deposited.^{43,44} Since the Neogene, the Pacific plate receded to the Eurasian subduction zone, the Dongpu Depression entered the stage of depression, and Guantao

Formation (Ng), Minghuazhen Formation (Nm), and Pingyuan Formation (Qp) deposited.⁴¹ Es₄ can be subdivided into Es₄^L (lower sub-formation) and Es₄^U (upper sub-formation); Es₃ can be subdivided into Es₃^L (lower sub-formation), Es₃^M (lower middle-formation), and Es₃^U (upper sub-formation); Es₂ can be subdivided into Es₂^L (lower sub-formation) and Es₂^U (upper sub-formation); and Es₁ can be subdivided into Es₁^L (lower sub-formation) and Es₁^U (upper sub-formation)⁴⁵ (Figure 2). The lithology varies from bottom to top: the lithology of the lower part of Es₄^U is dominated by magenta and gray mudstone interbedded with light brown sandstone, while that of the upper part is mainly the interbedded interval, which contains dark gray mud-shale and thin sandstone; the lithology of Es₃^L is the combination of dark gray mudstone, shale, gray silty sandstone, gray silty mudstone, and gray argillaceous silty sandstone; that of Es₃^M is

Table 1. Geochemical Data and Lithologies of the Samples from SA and NA in the Dongpu Depression^a

number	well	depth (m)	location	formation	lithology	TOC (%)	T_{max} (°C)	S_1 (mg/g)	S_2 (mg/g)	$S_1 + S_2$ (mg/g)	HI (mg/g of TOC)	R_o (%)
1	W146	2838.00	SA	Es ₄ ^U	dark gray shale	3.34	432.0	0.85	22.16	23.01	663.08	
2 ^b	W146	2838.90	SA	Es ₄ ^U	dark gray mudstone	3.29	431.6	0.67	20.62	21.29	625.97	0.55
3	W146	2840.85	SA	Es ₄ ^U	dark gray shale	1.98	440.0	0.49	11.24	11.73	568.54	
4	W146	2842.55	SA	Es ₄ ^U	gray shale	0.76	437.0	0.10	0.89	0.99	117.88	
5	W146	2846.65	SA	Es ₄ ^U	dark gray shale	1.19	440.0	0.41	5.91	6.32	497.47	0.56
6	W146	2852.56	SA	Es ₄ ^U	dark gray shale	1.52	436.0	0.57	6.41	6.98	421.16	
7	W146	2855.20	SA	Es ₄ ^U	dark gray shale	1.20	437.0	0.36	4.93	5.29	410.15	
8	W146	2873.55	SA	Es ₄ ^U	dark gray shale	1.22	439.0	0.56	4.82	5.38	394.11	
9	W146	2880.48	SA	Es ₄ ^U	dark gray shale	1.09	428.0	0.90	2.49	3.39	228.02	
10	W20	2640.50	SA	Es ₃ ^M	brown oil shale	6.51	436.0	1.23	39.78	41.01	629.57	
11	W20	2647.50	SA	Es ₃ ^M	dark gray mudstone	0.82	434.0	0.54	2.04	2.58	315.79	
12	W20	2652.30	SA	Es ₃ ^M	gray mudstone	3.49	435.0	1.16	19.70	20.86	597.71	
13	W20	2657.10	SA	Es ₃ ^M	gray mudstone	2.17	432.0	0.57	7.60	8.17	377.02	
14	W20	2693.30	SA	Es ₃ ^L	dark gray mudstone	2.24	417.0	0.79	5.55	6.34	282.91	
15	W20	2708.40	SA	Es ₃ ^L	dark gray shale	0.51	430.0	0.06	0.66	0.72	140.35	
16	W305	2773.00	SA	Es ₃ ^L	dark gray shale	0.67	426.0	0.02	2.07	2.09	311.94	0.60
17	W324	2729.35	SA	Es ₃ ^L	dark gray shale	1.27	436.0	0.42	5.39	5.81	457.48	
18	W324	2730.34	SA	Es ₃ ^L	dark gray shale	2.56	440.0	0.44	17.17	17.61	687.89	
19	W324	2732.08	SA	Es ₃ ^L	dark gray shale	1.29	436.0	0.14	5.32	5.46	424.24	
20	W324	2832.50	SA	Es ₃ ^L	dark gray shale	0.94	444.0	0.01	3.85	3.86	410.64	
21	W325	3067.50	SA	Es ₃ ^M	dark gray shale	1.84	434.0	0.12	7.08	7.20	391.30	0.69
22	W388	2930.00	SA	Es ₃ ^M	dark gray shale	0.76	433.0	0.10	1.81	1.91	252.31	
23	W388	2996.00	SA	Es ₃ ^L	gray mudstone	0.82	437.0	0.07	1.63	1.70	207.32	0.66
24	W388	3058.00	SA	Es ₃ ^L	dark gray shale	0.71	435.0	0.08	1.85	1.93	273.37	
25	W388	3224.00	SA	Es ₃ ^L	oil shale	0.90	440.0	0.14	2.69	2.83	315.50	
26	W42	3276.78	SA	Es ₃ ^M	dark gray mudstone	0.59	435.0	0.10	0.49	0.59	100.00	
27	W42	3455.77	SA	Es ₃ ^M	dark gray mudstone	0.41	443.0	0.04	0.32	0.36	87.17	
28	W79	3103.78	SA	Es ₃ ^M	dark gray mudstone	0.38	428.0	0.09	0.16	0.25	65.82	0.70
29	W79	3106.53	SA	Es ₃ ^M	dark gray mudstone	0.41	429.0	0.04	0.15	0.19	46.76	
30	W79	3186.48	SA	Es ₃ ^M	dark gray mudstone	0.50	438.0	0.03	0.10	0.13	26.02	0.73
31	W79	3191.98	SA	Es ₃ ^M	dark gray mudstone	0.52	435.0	0.08	0.24	0.32	61.16	
32	X6	3395.80	NA	Es ₃ ^M	dark gray mudstone	0.17	432.0	0.01	0.13	0.14	84.36	0.98
33	X6	3397.50	NA	Es ₃ ^M	mulberry mudstone	0.25	446.5	0.01	0.13	0.14	57.34	
34	X7	4393.56	NA	Es ₃ ^L	gray mudstone	0.44	477.0	0.01	0.07	0.08	18.54	1.60
35	X7	4394.31	NA	Es ₃ ^L	dark gray mudstone	0.21	448.0	0.01	0.01	0.02	7.53	
36	X7	4397.88	NA	Es ₃ ^L	gray mudstone	0.29	460.0	0.03	0.27	0.30	104.93	
37	X7	4398.85	NA	Es ₃ ^L	dark gray mudstone	0.20	450.0	0.01	0.00	0.01	7.04	
38	X8	3155.16	NA	Es ₃ ^M	dark gray mudstone	0.17	445.3	0.00	0.00	0.01	3.49	
39 ^b	X8	3156.80	NA	Es ₃ ^M	dark gray mudstone	0.39	439.0	0.00	0.24	0.24	61.04	0.88
40	X8	3208.35	NA	Es ₃ ^M	dark gray mudstone	0.32	447.7	0.00	0.04	0.04	13.47	
41	X8	3856.76	NA	Es ₃ ^L	gray mudstone	0.52	455.1	0.02	0.15	0.17	32.12	
42	X12	4664.87	NA	Es ₃ ^L	dark gray mudstone	0.41	452.0	0.01	0.23	0.24	58.68	1.82
43	X14	4234.90	NA	Es ₃ ^L	gray mudstone	0.24	458.6	0.02	0.12	0.14	58.30	
44	X14	4235.95	NA	Es ₃ ^L	gray mudstone	0.42	440.3	0.09	0.32	0.41	95.99	
45	X14	4236.50	NA	Es ₃ ^L	gray mudstone	0.74	439.2	0.49	0.91	1.40	189.04	
46	X14	4237.70	NA	Es ₃ ^L	dark gray mudstone	0.75	443.3	0.31	0.81	1.12	149.40	

Table 1. continued

number	well	depth (m)	location	formation	lithology	TOC (%)	T_{\max} (°C)	S_1 (mg/g)	S_2 (mg/g)	$S_1 + S_2$ (mg/g)	HI (mg/g of TOC)	R_o (%)
47	X14	4238.75	NA	Es ₃ ^L	dark gray mudstone	0.85	439.5	0.39	0.86	1.26	147.41	
48	X14	4239.80	NA	Es ₃ ^L	dark gray mudstone	0.51	445.0	0.16	0.41	0.57	112.58	
49	X14	4241.00	NA	Es ₃ ^L	dark gray mudstone	0.46	448.5	0.09	0.35	0.44	95.31	
50	X14	4241.60	NA	Es ₃ ^L	dark gray mudstone	0.83	449.0	0.23	0.60	0.84	101.02	
51	X14	4330.45	NA	Es ₃ ^L	dark gray mudstone	0.36	462.5	0.02	0.19	0.21	58.32	
52	X14	4332.05	NA	Es ₃ ^L	dark gray mudstone	0.55	435.0	0.19	0.89	1.08	196.19	
53	X14	4408.90	NA	Es ₃ ^L	dark gray mudstone	0.29	445.5	0.02	0.19	0.21	72.45	1.61

^aSA and NA represent the saline area and non-saline area in the Dongpu Depression, respectively. HI represents the hydrogen index, which is the ratio of $100S_2/TOC$. ^bSamples used for closed gold cube thermal simulation experiments.

composed of dark gray mudstone and salt rocks; the lithology of Es₃^L is mainly gray mudstone and light gray siltstone; and that of Es₂ is mainly purple mudstone that mixed with siltstone or sandy mudstone. The lithology of Es₁ is dominated by gray mudstone and light gray siltstone (the lithological description is from the Zhongyuan Oilfield, SINOPEC) (Figure 2).

The effective hydrocarbon source rocks and thick saline rocks are widely distributed in the Es₃ and Es₄. In these two formations, in comparison to the OM in the NA of the southern area, that in the SA of the northern area has a higher abundance and a better type. In addition, the results of actual explorations also show that the oil and gas in the Dongpu Depression are mainly distributed in the SA.^{46,47}

It is of great significance to accurately recover the thermal evolution history of a basin for evaluating the hydrocarbon generation potential of the source rocks, and the reliable thermal history is a key factor in the application of hydrocarbon generation kinetics to practical geological conditions.^{48,49} In comparison to the use of R_o and paleo-geothermics, the geothermal gradient of the Paleogene in the Dongpu Depression calculated by the apatite fission track is moderate, at about 3.6 °C/100 m.⁴⁸ The Dongying Movement at the end of the Paleogene caused the overall uplift of Dongpu Depression to suffer denudation, and the thickness of this denudation in the Ed is about 800–1200 m.⁵⁰ The geothermal gradient was 3.6–3.8 °C/100 m in the end of Ed and then reduced to 3.4–3.5 °C/100 m as a result of the denudation period. In the early Neogene, because the strata gradually covered the denudation surface in the whole area, the geothermal gradient increased, reaching 3.6–3.7 °C/100 m at the end of Ng, and then the geothermal gradient gradually decreased because the depression was in the depression stage. Now, the geothermal gradient has decreased to 3.1–3.3 °C/100 m.⁵¹

3. SAMPLES AND EXPERIMENTS

3.1. Samples. A total of 53 samples (31 and 22 are distributed in SA and NA, respectively), including shale and mudstone, were selected from some typical wells (Figure 1). Then, Rock-Eval pyrolysis and total organic carbon (TOC) experiments are performed on these 53 samples, and vitreous component (R_o) analysis is performed on 12 samples. Finally, a shale sample in SA and a mudstone sample in NA were chosen for the gold tube thermal simulation experiments.

3.2. Experiments. 3.2.1. Pyrolysis, R_o , and TOC. The Rock-Eval IV instrument is used for pyrolysis experiments. The samples are heated to 600 °C in the helium environment to generate S_1 and S_2 and obtain the parameter T_{\max} . S_1 represents free hydrocarbon released at 300 °C; S_2 represents pyrolytic hydrocarbon released at 300–600 °C; and T_{\max} represents the temperature at which S_2 reaches the maximum value. LECO CS230 is used for the analysis of the TOC, and CRAIC is used for the acquirement of R_o .

3.2.2. Extraction of Kerogen. First, the samples are ground into powder (100 mesh) and then treated with HCl and HF to remove carbohydrates and silicates to obtain concentrated kerogen. Subsequently, the precipitated silica gel generated from the process of treatment by HF is removed by hot hydrochloric acid. Next, the organic residue is washed with distilled water to a neutral pH and separated by heavy liquid flotation to obtain kerogen. Finally, kerogen is heated at 100 °C for 24 h.⁵²

3.2.3. Thermal Simulation Experiments. According to the criterion (SY/T7035-2016), there are several requirements for gold tubes: the purity of gold is equal to or greater than 99%; the inner diameter is 4 mm; the length is 60 mm; the wall thickness is 0.25 mm; and there is no sand hole or crack.

Under the protection of argon (volume fraction is equal to or greater than 99%), about 10 g of kerogen sample is put into each gold tube and the wall of the tube should not be stained with the sample. After the remaining air is replaced with argon for 15 min, the tube is welded with an argon arc welding gun. Next, the gold tube is placed in the high-pressure kettle and filled with water by the high-pressure pump. The high-pressure water causes the flexible deformation of the gold tube to exert pressure on the sample. The pressure is set at 50 MPa (error is less than 0.5 MPa). Subsequently, the sample is heated from room temperature to 200 °C for 10 h and then heated to the desired simulation temperature (300–600 °C) at the heating rates of 2 and 20 °C/h, respectively, and at the final constant temperature (300–600 °C) for some time. Each heating curve has 12 temperature points (number of tubes is 12) with an interval of heating at 24 °C (error is less than 1 °C).

3.3.4. Gas Chromatography (GC) Analysis. After taking out the samples, the gases (C_{1-5} , CO_2 , etc.) are released in the vacuum system of gold tubes, which is connected with GC7890 gas chromatography online, to complete the analysis of all gases.⁵³ The light hydrocarbons (C_{6-14}) are frozen with liquid nitrogen and then collected. After 5 min, 2 mL of dichloromethane solvent is quickly added and the gold tubes are cut open. The gold tubes and the samples are sealed and refrigerated for use. Next, the light hydrocarbon collection bottles containing the gold tube and samples are oscillated and ultrasonically extracted for 2 min, and the deuterium internal standard solution (50 μ L) is added to the bottle. Those mixtures are shaken evenly and settled to subside, before

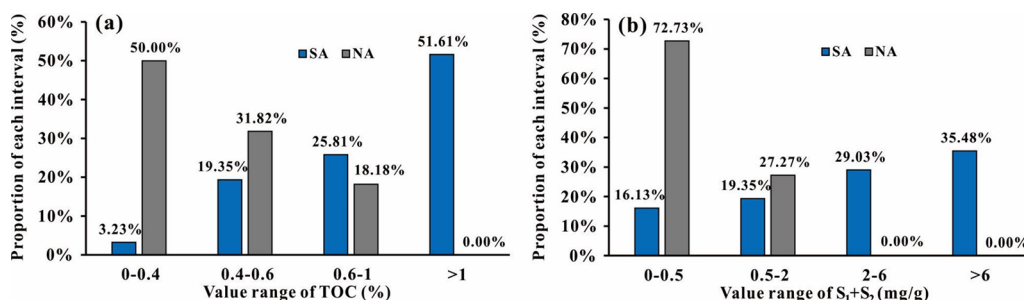


Figure 3. (a) Plot of ratios of several intervals of TOC values to the total number of samples in SA and NA, separately, and (b) plot of ratios of several intervals of $S_1 + S_2$ values to the total number of samples in SA and NA, separately. SA and NA represent the saline area and non-saline area of the Dongpu Depression.

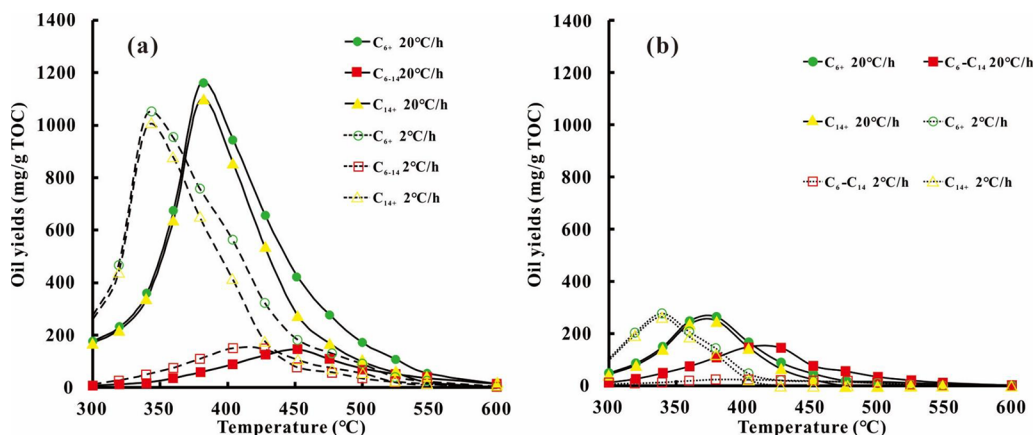


Figure 4. (a) Oil yields (C_{6+} , C_{6-14} , and C_{14+}) of the SA sample with an increasing temperature at heating rates of 2 and 20 °C/h in the closed gold tube thermal simulation experiments and (b) oil yields (C_{6+} , C_{6-14} , and C_{14+}) of the NA sample with an increasing temperature at heating rates of 2 and 20 °C/h in the closed gold tube thermal simulation experiments. SA and NA represent the saline area and non-saline area of the Dongpu Depression.

transferring 1 mL of the clarified solution to a 2 mL chromatographic bottle.

The specification of a HP5 chromatographic column is 50 m × 0.32 mm × 0.25 μm, and the flow rate of the column is 1.5 mL/min. The heating procedure of the column box is that the temperature is maintained at 40 °C for 5 min and then increases to 290 °C, at a heating rate of 4 °C/min, which is maintained for 15 min. The inlet temperature is 290 °C, and the detector temperature is 300 °C. The injection volume is 1 μL. The injection mode is automatic injection without a shunt.

After gas chromatographic analysis of light hydrocarbon (C_{6-14}) in accordance with the above conditions, the remaining solution in the chromatographic bottle is poured back into the original light hydrocarbon collection bottle. The dichloromethane solution in the light hydrocarbon collection bottle, together with the gold tube and samples, is shaken by an ultrasonic wave for 2 min to be extracted, and then this mixture is filtrated by the organic filtration membrane with a diameter of 0.45 μm. The previous step is repeated until the filtrate is below the 3rd fluorescence level. Finally, the filtrate was volatilized to dry at 40 °C and weighed to a constant weight (at an interval of 30 min, the difference in weigh is less than 0.1 mg) with a balance to obtain C_{14+} .

3.3.5. Gas Chromatography–Isotope Ratio Mass Spectrometry (GC–IRMS) Analysis. A thermal simulation gas carbon isotope is analyzed in a GC–IRMS isotope mass spectrometer of Isochrom II type [analysis error of ±0.3‰ Pee Dee Belemnite (PDB)], and the chromatographic column of Poraplot Q type (30 m × 0.32 mm × 0.25 mm) is used with helium as the carrier gas. Then, the heating program is set up: the initial temperature is 50 °C, and this temperature is constant for 3 min. Then, the temperature increases to 150 °C at a rate of 4 °C/min, and this temperature is constant for 8 min.

4. RESULTS

4.1. OM Abundance, Type, and Maturity. The TOC values of 31 SA samples are 0.38–6.51% (mean of 1.48%), and those of 22 NA samples are 0.17–0.85% (mean of 0.43%). More than 75% of the SA samples have a TOC value greater than 0.6%, and more than 50% of the SA samples have a TOC value greater than 1%. About 80% of the NA samples have a TOC value less than 0.6% (Table 1 and Figure 3a). The $S_1 + S_2$ values of 31 SA samples are 0.13–41.01 mg/g (mean of 6.98 mg/g), and those of 22 NA samples are 0.01–1.40 mg/g (mean of 0.41 mg/g). About 65% of the SA samples have a $S_1 + S_2$ value greater than 2 mg/g, and all NA samples have a $S_1 + S_2$ value less than 0.6% (Table 1 and Figure 3b). The hydrogen index (HI) values ($100S_2/TOC$) of 31 SA samples are 26.02–687.89 mg/g of TOC (mean of 335.12 mg/g of TOC), and those of 22 NA samples are 3.49–196.19 mg/g of TOC (mean of 378.39 mg/g of TOC) (Table 1). The R_o and T_{max} values of all samples are 0.55–1.82% (mean of 0.68%) and 417–477 °C, respectively, which show that the source rock has entered the mature stage and the samples for thermal simulation experiments are relatively low-mature rocks (Table 1). The difference of TOC, $S_1 + S_2$, and HI values between SA and NA samples exhibits the difference of the hydrocarbon generation potential, which can contribute to highlight the significance of source rocks in SLRBs.

4.2. Hydrocarbon Yields. **4.2.1. Oil Yields.** As shown in panels a and b of Figure 4 and Table 2, the oil (C_{6+}) yield of the SA sample peaks at about 380₂₀ °C/h (1155.94₂₀ °C/h

Table 2. Hydrocarbon Yield Data of the SA Shale and NA Mudstone Kerogen Samples

number	weight (mg)	T (°C)	easy R_o (%)	20 °C/h										$\delta^{13}C_1 - \delta^{13}C_2$ (‰)	$\ln(C_1/C_2)$	$\ln(C_2/C_3)$
				C_1 (mg/g)	C_{6-14} (mg/g)	C_{14+} (mg/g)	C_{6+} (mg/g)	C_{1-5} (mg/g)	C_{2-5} (mg/g)	$\delta^{13}C_1$ (‰)	$\delta^{13}C_2$ (‰)	$\delta^{13}C_3$ (‰)				
W146-1	98.53	300.00	0.44	0.25	6.37	169.80	176.17	0.37	0.12	-48.75	-27.94	-27.02	2.20	0.64		
W146-2	88.33	320.00	0.51	0.59	10.21	220.33	230.53	1.08	0.49	-44.81	-29.33	-26.88	1.72	0.44		
W146-3	79.96	340.00	0.59	1.32	19.31	338.87	358.18	2.70	1.38	-44.91	-29.15	-26.72	1.40	0.55		
W146-4	69.26	360.00	0.68	2.92	33.58	639.73	673.31	7.69	4.77	-42.03	-28.87	-25.69	1.02	0.53		
W146-5	59.60	380.00	0.77	8.07	58.56	1097.38	1155.94	21.23	13.17	-39.23	-27.94	-25.03	0.65	0.49		
W146-6	58.27	404.00	0.92	13.00	87.98	855.10	943.09	47.29	34.29	-37.91	-26.87	-25.29	0.70	0.41		
W146-7	50.70	428.00	1.15	26.82	124.10	531.41	655.51	96.90	70.08	-37.26	-27.02	-24.76	0.67	0.35		
W146-8	48.22	452.00	1.42	45.23	146.24	273.98	420.22	167.58	122.35	-36.11	-27.45	-24.76	0.75	0.32		
W146-9	45.74	476.00	1.75	83.60	108.00	166.49	274.50	294.73	211.12	-34.82	-25.18	-20.41	0.84	0.39		
W146-10	39.35	500.10	2.13	140.26	72.51	98.23	170.74	420.99	280.73	-32.36	-22.28	-14.43	1.05	0.73		
W146-11	29.87	524.90	2.54	205.08	51.48	55.37	106.84	454.35	249.27	-31.88	-18.11	-2.05	1.35	1.59		
W146-12	20.63	548.40	2.99	285.31	34.41	19.58	53.99	469.11	183.80	-27.06	-2.29		3.08	4.39		
W146-13	10.94	599.70	3.87	416.16	13.88	0.00	13.88	452.88	36.72							
W146-14	77.08	299.30	0.56	0.82	12.38	252.73	265.12	1.59	0.77	-49.26	-29.00	-26.70	1.60	0.40		
W146-15	79.91	319.40	0.65	2.09	26.13	439.68	465.81	4.98	2.89	-46.62	-29.88	-26.81	1.14	0.53		
W146-16	70.54	339.50	0.75	5.12	48.23	986.35	1034.57	18.22	13.10	-41.90	-29.54	-25.73	0.73	0.42		
W146-17	66.24	359.80	0.86	12.06	74.63	878.22	952.85	44.77	32.71	-41.44	-28.41	-25.19	0.60	0.52		
W146-18	62.83	379.50	1.04	21.87	108.68	649.49	758.18	73.62	51.75	-37.89	-27.09	-24.67	0.68	0.58		
W146-19	56.54	403.90	1.31	40.12	149.22	413.59	562.81	131.77	91.65	-37.42	-26.11	-24.84	0.79	0.47		
W146-20	48.22	427.90	1.63	75.11	145.39	175.48	320.87	239.47	164.35	-35.82	-26.71	-25.13	0.85	0.40		
W146-21	44.25	452.10	2.02	117.42	76.14	105.17	181.32	374.67	257.25	-32.73	-26.84	-23.24	0.84	0.36		
W146-22	50.27	477.50	2.49	183.95	56.01	72.68	128.69	442.09	258.14	-31.63	-23.69	-17.20	1.02	0.58		
W146-23	41.36	500.00	2.91	263.42	33.77	54.40	88.17	453.75	190.33	-30.69	-19.43	-7.07	1.34	1.23		
W146-24	31.67	524.20	3.38	354.36	20.75	18.82	39.57	466.75	112.39	-31.46	-12.11		1.92	2.27		
W146-25	20.99	548.00	3.80	420.15	11.77	10.08	21.85	458.57	38.42	-29.50	-3.58		3.04	4.28		
W146-26	10.35	599.70	4.45	462.84	1.14	0.00	1.14	465.56	2.72	-25.99			5.79	4.31		
X8-1	100.52	300.00	0.44	0.08	4.88	43.34	48.22	0.15	0.07				1.46	0.44		
X8-2	90.38	320.00	0.51	0.19	6.76	78.87	85.64	0.47	0.28				1.12	0.15		
X8-3	80.41	340.00	0.59	0.35	8.52	140.37	148.89	0.80	0.45				1.35	0.20		
X8-4	70.42	360.00	0.68	0.80	11.27	236.21	247.48	1.93	1.03				1.33	0.30		
X8-5	60.45	380.00	0.77	1.75	14.60	248.96	263.56	4.77	3.02				1.08	0.40		
X8-6	60.38	404.00	0.92	3.87	20.24	145.94	166.18	10.35	6.48				0.96	0.57		
X8-7	50.59	428.00	1.15	9.01	24.05	64.58	88.63	19.98	10.96	-43.63	-24.35	-22.72	1.14	0.79		
X8-8	50.44	452.00	1.42	15.46	22.88	23.56	46.43	29.44	13.98	-37.97	-22.94	-21.59	1.25	1.08		
X8-9	40.54	476.00	1.75	30.45	19.23	0.00	19.23	45.09	14.64	-35.74	-20.61	-19.10	1.80	1.23		
X8-10	40.30	500.10	2.13	49.33	15.96	0.00	15.96	56.96	7.62	-31.23	-14.44		2.67	2.13		
X8-11	30.29	524.90	2.54	58.95	10.73	0.00	10.73	60.46	1.51	-29.91			4.36	3.00		
X8-12	20.26	548.40	2.99	52.17	6.93	0.00	6.93	52.61	0.44	-26.78			5.48	2.79		
X8-13	10.84	599.70	3.87	39.02	1.61	0.00	1.61	39.39	0.37	-20.29			5.35	3.05		

Table 2. continued

number	weight (mg)	T (°C)	easy R_o (%)	C_1 (mg/g)	C_{6-14} (mg/g)	C_{14+} (mg/g)	C_{6+} (mg/g)	C_{1-5} (mg/g)	C_{2-5} (mg/g)	$\delta^{13}C_1$ (‰)	$\delta^{13}C_2$ (‰)	$\delta^{13}C_3$ (‰)	$\delta^{13}C_1 - \delta^{13}C_2$ (‰)	$\ln(C_1/C_2)$	$\ln(C_2/C_3)$
X8-14	90.65	299.30	0.56	0.21	6.79	93.93	100.72	0.43	0.22					1.41	0.28
X8-15	80.76	319.40	0.65	0.44	9.14	193.70	202.85	1.23	0.79					1.21	0.15
X8-16	70.55	339.50	0.75	1.47	12.80	263.84	276.64	3.94	2.47					1.10	0.38
X8-17	60.60	359.80	0.86	2.78	18.75	187.89	206.64	8.31	5.53					0.69	0.81
X8-18	50.57	379.50	1.04	7.43	23.64	119.43	143.07	17.89	10.46	-45.55	-24.77	-22.43	-20.78	1.00	0.79
X8-19	50.63	403.90	1.31	16.26	23.22	23.47	46.69	30.39	14.14	-40.34	-22.85	-20.95	-17.49	1.31	1.05
X8-20	50.76	427.90	1.63	30.08	20.58	0.00	20.58	46.14	16.05	-35.14	-20.47	-18.72	-14.67	1.68	1.28
X8-21	41.03	452.10	2.02	53.60	17.86	0.00	17.86	66.95	13.36	-32.85	-15.73	-13.66	-17.11	2.25	1.84
X8-22	40.71	477.50	2.49	68.35	14.67	0.00	14.67	71.54	3.19	-28.39	-5.13			3.75	3.22
X8-23	30.69	500.00	2.91	82.01	10.21	0.00	10.21	82.61	0.61	-26.69				5.61	2.93
X8-24	30.48	524.20	3.38	71.67	4.82	0.00	4.82	71.96	0.28	-23.08				6.25	2.81
X8-25	20.64	548.00	3.80	57.86	2.07	0.00	2.07	58.15	0.29	-22.51				5.99	2.91
X8-26	10.50	599.70	4.45	76.27	0.86	0.00	0.86	76.35	0.08	-29.97				7.47	

^aSA and NA represent the saline area and no.-saline area in the Dongpu Depression, respectively, and 20 and 2 °C/h represent two different heating rates. Yield unit: mg of hydrocarbon (HC)/g of TOC.

mg/g of TOC) and peaks at about 340 °C (1034.57₂ °C/h mg/g of TOC) and that of the NA sample peaks at about 380₂₀ °C/h °C (263.56₂₀ °C/h mg/g of TOC) and peaks at about 340₂ °C/h °C (276.64₂ °C/h mg/g of TOC) (the lower right corner “₂₀°C/h” and “₂°C/h” represent “at the heating rate of 20 °C/h” and “at the heating rate of 2 °C/h”, respectively). However, the oil yields in both marine and lacustrine oil-prone source rocks are generally 300–600 mg/g of TOC.⁵⁴ It can be known that the SA sample has a higher oil yield and the NA sample has a lower oil yield, which is in line with the proven reserves in the Dongpu Depression. In addition, the two critical points (380₂₀ °C/h and 340₂ °C/h °C) represent the balance between kerogen cracking into oil and oil secondary cracking.

The heavy oil (C_{14+}) yield of the SA sample peaks at about 380₂₀ °C/h °C (1097.38₂₀ °C/h mg/g of TOC) and at about 340₂ °C/h °C (986.35₂ °C/h mg/g of TOC), and that of the NA sample peaks at about 380₂₀ °C/h °C (248.96₂₀ °C/h mg/g of TOC) and at about 340₂ °C/h °C (263.84₂ °C/h mg/g of TOC). Furthermore, the value of C_{14+} is slighter less than that of C_{6+} , which can testify that the components of oil cracking from kerogen are mainly heavy oil (C_{14+}).

The light oil (C_{6-14}) yield gradually increases until 452₂₀ °C/h and 403₂ °C/h °C for the SA sample and 428₂₀ °C/h and 379.50₂ °C/h °C for the NA sample, respectively, and then starts to decrease. Before this critical point (452₂₀ °C/h and 403₂ °C/h °C for SA and 428₂₀ °C/h and 379.5₂ °C/h °C for NA), the heavy oil (C_{14+}) yield has already begun to decrease substantially at 380₂₀ °C/h and 340₂ °C/h °C (panels a and b of Figure 4), which shows that the reaction of kerogen cracking into C_{14+} is very slight and C_{14+} cracking into C_{6-14} is intense. Moreover, although heavy oil (C_{14+}) continues to decrease, the gas from oil cracking can be ignored as long as light oil (C_{6-14}) does not reach its maximum value; that is, there is almost no gas generated from the oil secondary cracking during the intervals from 380₂₀ °C/h to 452₂₀ °C/h °C and from 340₂ °C/h to 403₂ °C/h °C for the SA sample and that from 380₂₀ °C/h to 428₂₀ °C/h °C and from 340₂ °C/h to 379.5₂ °C/h °C for the NA sample. After this critical point (452₂₀ °C/h and 403₂ °C/h °C for SA and 428₂₀ °C/h and 379.5₂ °C/h °C for NA), the decrease of the C_{6-14} yield can be attributed to the intense process of oil secondary cracking. In the closed system, when the amount of oil generated from kerogen cracking is less than that of oil secondary cracking, the C_{6+} yield increases, which shows the stage of mass gas generation.

4.2.2. Gas Yields. As shown in panels a and c of Figure 5 and Table 3, at two heating rates, the curve of the C_{1-5} yield increases significantly first and then tends to be relatively steady. More specifically, the C_{1-5} yield peaks at 548.4₂₀ °C/h °C (469.11₂₀ °C/h mg/g of TOC) and 524₂ °C/h °C (466.75₂ °C/h mg/g of TOC) for the SA sample and at 524.9₂₀ °C/h °C (60.46₂₀ °C/h mg/g of TOC) and 500₂ °C/h °C (82.61₂ °C/h mg/g of TOC) for the NA sample. In contrast, the C_{2-5} yield gradually increases until it reaches the maximum at about 500₂₀ °C/h °C (280.73₂₀ °C/h mg/g of TOC) and at 477.5₂ °C/h °C (258.14₂ °C/h mg/g of TOC) for the SA sample and at about 476₂₀ °C/h °C (14.64₂₀ °C/h mg/g of TOC) and at 427.9₂ °C/h °C (16.05₂ °C/h mg/g of TOC) for the NA sample. After the peak temperature, C_{2-5} starts to crack substantially to cause the decline of its yield. Meanwhile, the C_{6+} (C_{6-14} and C_{14+}) yields still decrease, which illustrates that the action of oil cracking is still going on (panels a and b of Figure 4). Additionally, taking an example of the results of the SA sample at the heating rate of 20 °C/h, the five curves show that the C_5 ,

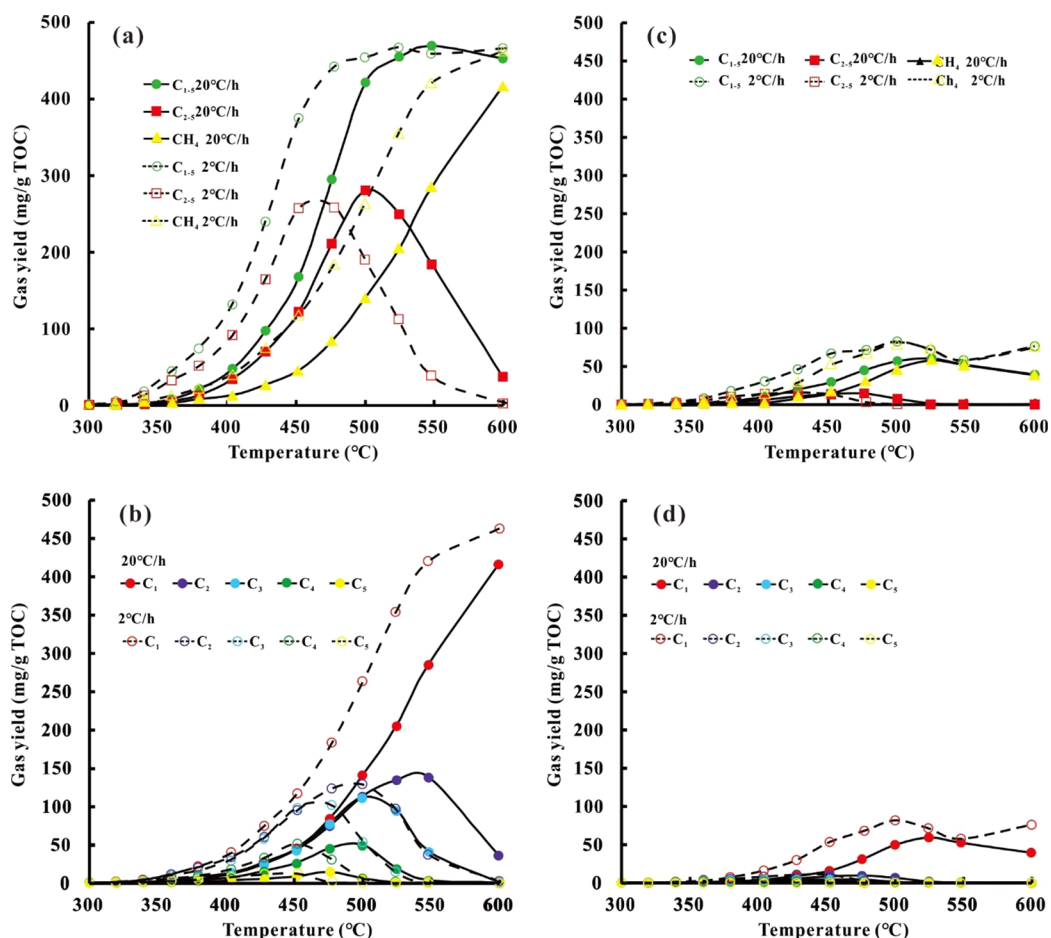


Figure 5. Gas yield of SA and NA samples with an increasing pyrolysis temperature at heating rates of 2 and 20 °C/h: (a) total gases (C_{1-5}), wet gases (C_{2-5}), and CH_4 yield of the SA sample at two heating rates, (b) C_1 , C_2 , C_3 , C_4 , and C_5 yields of the SA sample at the heating rates of 20 °C/h, (c) C_1 , C_2 , C_3 , C_4 , and C_5 yields of the SA sample at the heating rates of 2 °C/h, (d) total gases (C_{1-5}), wet gases (C_{2-5}), and CH_4 yield of the NA sample at two heating rates, (e) C_1 , C_2 , C_3 , C_4 , and C_5 yields of the NA sample at the heating rates of 20 °C/h, and (f) C_1 , C_2 , C_3 , C_4 , and C_5 yields of the NA sample at the heating rates of 2 °C/h. SA and NA represent the saline area and non-saline area of the Dongpu Depression, respectively.

Table 3. Ranges of R_0 Values of Four Gas Evolution (Source) Stages in Different Source Socks

sample	gas evolution process (gas source) based on easy R_0 (%)			
	kerogen cracking ($C_1 < C_2$)	kerogen cracking ($C_1 > C_2$)	oil cracking	wet gas cracking
SA	0.6–1.0	1.0–2.2	2.2–3.8	3.8–4.5
C	0.7–1.1	1.1–1.4	1.4–3.0	3.0–4.5
CM	0.7–0.9	0.9–1.1	1.1–2.5	2.5–4.5
MS	0.7–0.9	0.9–1.7	1.7–3.9	3.9–4.4

^aSA and NA represent the saline area and non-saline area in the Dongpu Depression, respectively. MS is short for marine shale (data from Wang et al.⁶⁵); CM is short for coal measure mudstone (data from Zhao et al.⁴⁵); C is short for coal (data from Zhao et al.⁴⁵); and SA is short for saline lacustrine shale (this study). Those samples are used for the similar closed gold tube thermal simulation experiments.

C_4 , C_3 , and C_2 yields peak in turn at about 475, 495, 505, and 545 °C, respectively. It can be concluded that the trend of the C_{2-5} yield can be attributed to the joint effort of oil secondary cracking into C_{2-5} and C_{2-5} cracking into lighter gases, including CH_4 , C_2 , C_3 , and C_4 , after the critical temperature (500_{20 °C/h} or 477.5_{2 °C/h} °C) (panels b and d of Figure 5).

The CH_4 yield increases noticeably with the increasing temperature, and the final yield is slightly less than the C_{1-5} yield at about 416.16_{20 °C/h} mg/g of TOC and 462.84_{20 °C/h} mg/g for the SA sample and 39.02_{20 °C/h} mg/g of TOC and 76.27_{2 °C/h} mg/g for the NA sample, which indicates that if the R_0 or temperature is high enough, C_{2-5} can almost completely crack into CH_4 and the main component of gases is CH_4 . If the C_{2-5} cracking is the only source of CH_4 , the C_{1-5} yield must decrease because the C_{2-5} cracking can form not only lighter gases (CH_4 , C_2 , C_3 , and C_4) but also pyrobitumen. However, the experimental results show that there is no notable decrease in the curve of the C_{1-5} yield, which shows the existence of kerogen primary cracking.

4.2.3. Stable Carbon Isotope of Gas Components. The stable carbon isotope data of the NA sample have not been detected with enough valid data, and the $\delta^{13}C$ curves are similar at two heating rates (20 and 2 °C/h); therefore, the 20 °C/h data of the SA sample is henceforth used in describing the stable carbon isotopic fractionations evident with pyrolysis in this part. The initial value of $\delta^{13}C_3$ at 300 °C is -26.07% , which is similar to the average value of $\delta^{13}C$ (-26.02%).⁵⁵ The $\delta^{13}C_3$ and $\delta^{13}C_2$ values are greater than the average value (-26.02%) when the temperature is above 452 °C. The $\delta^{13}C_1$ value is almost less than the average value (-26.02%) and

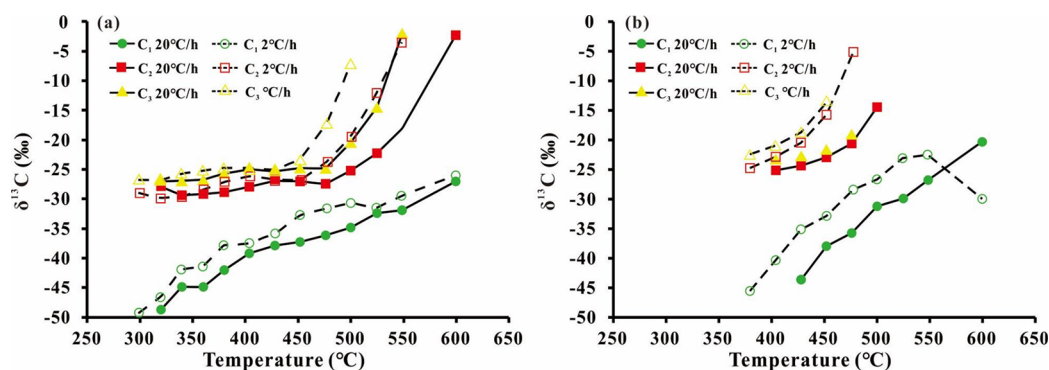


Figure 6. (a) Stable carbon isotope values of C_1 , C_2 , and C_3 with an increasing temperature at the heating rates of 20 and 20 °C/h for the SA shale sample and (b) stable carbon isotope values of C_1 , C_2 , and C_3 with an increasing temperature at the heating rates of 20 and 20 °C/h for the NA mudstone sample. SA and NA represent the saline area and non-saline area of the Dongpu Depression, respectively.

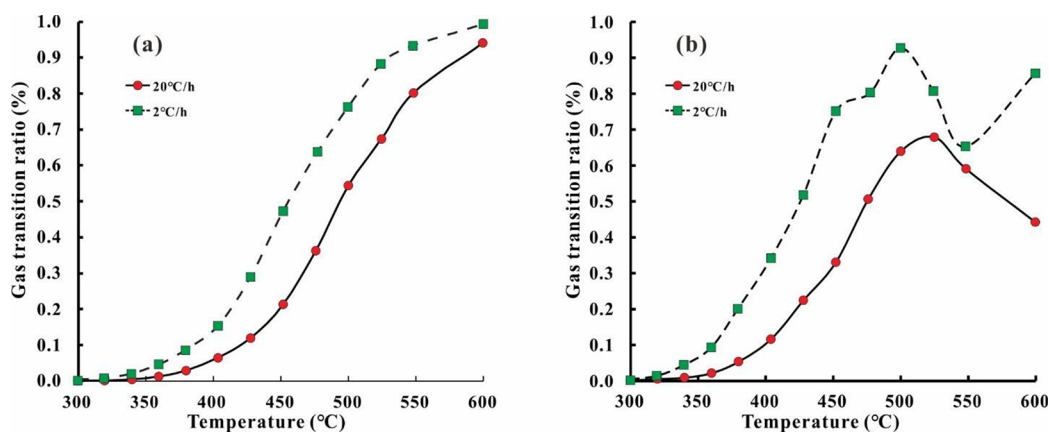


Figure 7. (a) Transition ratio of the total gases (C_{1-5}) with an increasing temperature at the heating rates of 20 and 20 °C/h for the SA shale sample and (b) transition ratio of the total gases (C_{1-5}) with an increasing temperature at the heating rates of 20 and 20 °C/h for the NA mudstone. SA and NA represent the saline area and non-saline area of the Dongpu Depression, respectively.

gradually tends to be -26.02‰ with the increasing temperature (panels a and b of Figure 6).

The trend of $\delta^{13}C_1$ gradually increases with the increasing temperature, which illustrates that the initial precursors of CH_4 are isotopically more depleted than the more thermally stable aromatic structures of kerogen.^{56,57} The $\delta^{13}C_3$ and $\delta^{13}C_2$ values remain relatively constant below 450 °C, but both start to increase above 450 °C. Moreover, propane (C_3) showed a more rapid ^{13}C enrichment than ethane (C_2) with the increasing temperature. This phenomenon illustrates preferential cracking of $^{12}C-^{12}C$ bonds, such that the non-cracked residue of C_2 and C_3 is isotopically heavy. The heavier $\delta^{13}C_3$ and $\delta^{13}C_2$ values can be attributed to the gases cracking at high temperatures.^{56,57}

As shown in Figure 6, at two heating rates, the distribution patterns of the $\delta^{13}C$ values for C_1 , C_2 , and C_3 are similar. Across the whole temperature range, there is a normal carbon isotope order, that is, $\delta^{13}C_3 > \delta^{13}C_2 > \delta^{13}C_1$. After summarization of previous relevant studies, Peng et al.⁵⁸ conclude that there is no obvious isotope inversion phenomenon in the confined system. However, the results of the same experiments on solid bitumen⁵⁹ and crude oil⁶⁰ show the phenomenon of gas isotope inversion ($\delta^{13}C_2 > \delta^{13}C_3 > \delta^{13}C_1$). This is an interesting phenomenon and needs to be further studied specifically.

4.3. Kinetic Parameters. To obtain the activation energy and frequency factor (A), the gas yield (C_t) in different

temperatures and the maximum gas yield (C_{max}) need to be used to obtain the gas transformation ratio (C) according to the formula ($C = C_t/C_{max}$).⁵³ In this research, the yields of methane and total hydrocarbon gas at two heating rates are eventually steady, and we can assume that the samples have almost ceased to generate gases. Therefore, the experimental results can be used to calculate relevant parameters. An assumptive C_{max} can be input into the KINETICS, and then the software can calculate the error of the two curves at two heating rates of 2 and 20 °C/h. The C_{max} value is assumed repeatedly, and when the error is the smallest, this assumed value is considered to be correct. In this study, the value is 340 mL/g of sample for the SA sample and 13 mL/g of sample for the NA sample. The calculated results of the C value are shown in panels a and b of Figure 7.

The first-order kinetic models are widely applied in hydrocarbon generation with a single frequency factor and a distribution of activation energies.^{30,61–64} The results show that the gas yields calculated by kinetic parameters are in good agreement with the experimentally measured data (panels a and b of Figure 8). The activation energy values range from 49 to 74 kcal/mol for the SA sample and from 30 to 53 kcal/mol for the NA sample. The frequency factor value (A) of the SA sample is $1.93 \times 10^{14} \text{ s}^{-1}$, and that of the NA sample is $2.41 \times 10^9 \text{ s}^{-1}$. Moreover, the shapes of the activation energy curve for SA and NA samples are both relatively smooth, which

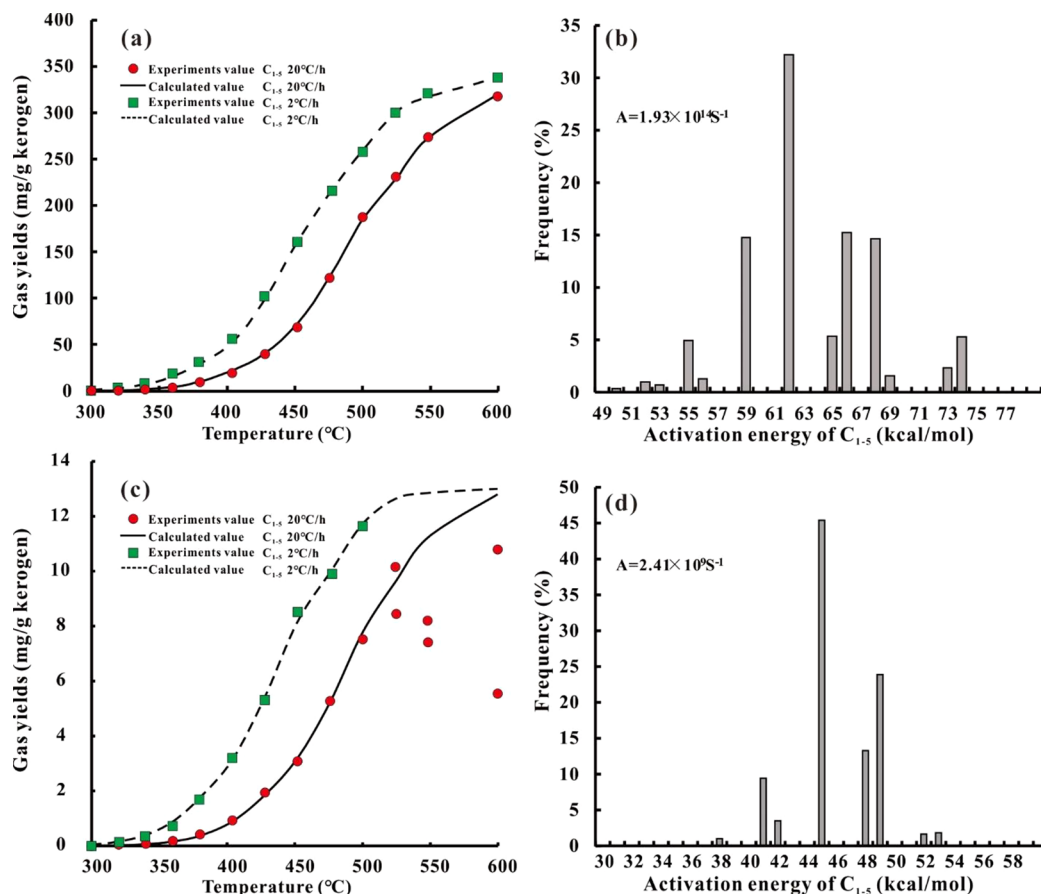


Figure 8. (a) Measured and calculated total gas (C_{1-5}) yield of the SA shale showing better curve fittings, (b) kinetic parameter sets for the generation of the total gases (C_{1-5}) of the SA shale, (c) measured and calculated total gas (C_{1-5}) yield of NA mudstone showing relatively poor curve fittings, and (d) kinetic parameter sets for the generation of the total gases (C_{1-5}) of NA mudstone. A represents the frequency factor value. SA and NA represent the saline area and non-saline area of the Dongpu Depression, respectively.

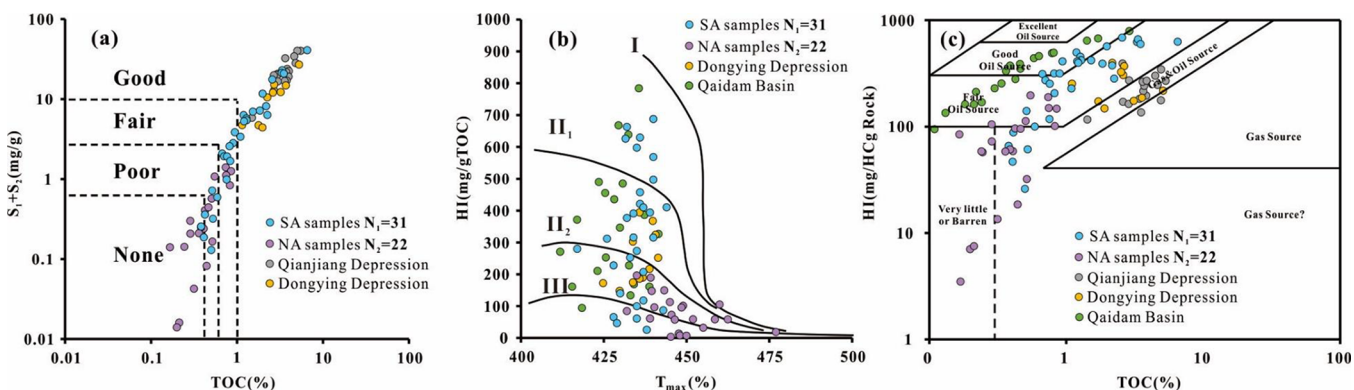


Figure 9. (a) TOC versus $S_1 + S_2$ plot showing that the quality of samples (the evaluation criterion is from Liu et al.⁵⁰), (b) HI versus T_{max} plot showing the kerogen types of samples (the evaluation criterion is from Liu et al.⁵⁰), and (c) HI versus TOC plot showing that samples are oil-prone. N_1 and N_2 represent the number of SA and NA samples, respectively. SA and NA represent the saline area and non-saline area of the Dongpu Depression, respectively.

shows that gas generation is a gradual process (panels c and d of Figure 8).

5. DISCUSSION

5.1. Oil-Prone Source Rocks in SLRBs. According to the evaluation criterion of lacustrine source rocks,⁶⁵ the plot of TOC versus HI was drawn, indicating that most SA samples are good source rocks and only a small part of NA source rocks are good source rocks (Figure 9a). In addition, the Paleogene

source rocks in the Dongying Depression⁶⁶ and Qianjiang Depression,⁶⁷ which are also typical SLRBs, are mainly good–extremely good (Figure 9a). Additionally, from the plot of T_{max} versus HI,⁵⁰ it can be concluded that the OM type of SA samples is dominated by II kerogen (II₁ and II₂), followed by I kerogen, and that of NA samples is mainly II₂ and III kerogen (Figure 9b). The OM type of source rocks in western Qaidam Basin,⁶⁸ which is also typical SLRBs, and that in the Dongying Depression⁶⁶ are dominated by II₁ and II₂ kerogen (Figure

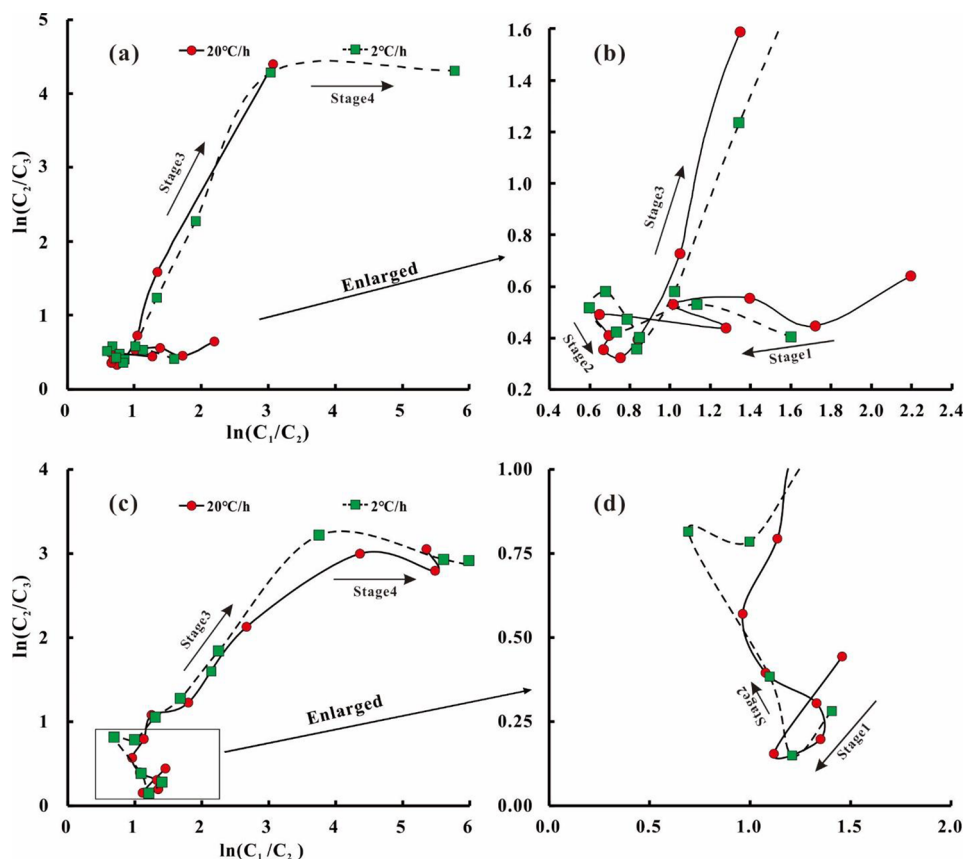


Figure 10. (a and b) Plot of $\ln C_2/C_3$ versus $\ln C_1/C_2$ for gases generated from the SA shale at the heating rates of 20 and 20 °C/h showing the process of gas evolution and (c and d) plot of $\ln C_2/C_3$ versus $\ln C_1/C_2$ for gases generated from NA mudstone at the heating rates of 20 and 20 °C/h showing the process of gas evolution. SA and NA represent the saline area and non-saline area of the Dongpu Depression, respectively.

9b). Those prove that source rocks in SLRBs are high-quality and tend to generate oil. Furthermore, the location of sample points from the Dongpu Depression (this study), Dongying Depression,⁶⁶ Qianjiang Depression,⁶⁷ and Qaidam Basin⁶⁸ in the plot of TOC versus HI also verify the oil-prone property of source rocks in SLRBs (Figure 9c). However, the values of C_{1-5} (gases) yields (peak values of 469.11_{20 °C/h} mg/g of TOC and 466.75_{2 °C/h} mg/g of TOC) (Figure 5 and Table 2) indicate that the source rocks in SLRBs have great potential of gas generation.

5.2. Gas Evolution during Experimental Pyrolysis.

According to the variation of hydrocarbon yields at different temperatures (easy R_o), the process of gas evolution can be preliminarily understood. Moreover, CH_4 is the main component of the total gas (Figure 5), and the gas stable carbon isotope compositions and yields of C_1 , C_2 and C_3 are widely used to distinguish whether CH_4 is directly sourced from kerogen or alternatively is a secondary product of oil cracking.^{56,69–72}

5.2.1. $\ln C_2/C_3$ and $\ln C_1/C_2$. The plot of $\ln(C_1/C_2)$ versus $\ln(C_2/C_3)$ based on yields of C_1 , C_2 , and C_3 is suitable for describing the dynamic process of the gas source: primary cracking of kerogen or secondary cracking of oil.⁷⁰ Generally, in the process of kerogen primary cracking, the value of C_1/C_2 increases progressively and the value of C_2/C_3 is constant (sometimes may slightly decrease or increase). In contrast, in the process of oil secondary cracking, the C_1/C_2 ratio is always constant and the value of C_2/C_3 increases noticeably with maturity (temperature or easy R_o).^{49,59,73}

As shown in Figure 10, because of the similar trend of the two heating curves, the results at the heating rate of 2 °C/h are used as examples to analyze. The gas generation process can be divided into four stages broadly.

5.2.1.1. SA Sample. Stage 1: when the temperature is between 300 and 379.5 °C (easy $R_o = 0.6–1.0\%$), $\ln C_1/C_2$ decreases significantly and $\ln C_2/C_3$ is constant at 0.5, which can be attributed to the occurrence of kerogen primary cracking. From this, it can be concluded that the order of preferential generation is $C_3 > C_2 > C_1$ with the consideration of C_{1-3} yields and the initial temperature of the reaction. Stage 2: at 379.5–452.10 °C (easy $R_o = 1.0–2.2\%$), the value of $\ln C_1/C_2$ increases and the value of $\ln C_2/C_3$ decreases slightly. This indicates that the typical cracking of kerogen generates more C_1 than C_2 , which can be attributed to the primary cracking of kerogen arylmethyl and terminal methyl.^{49,74} Stage 3: at the third stage (452.10–548 °C or easy $R_o = 2.2–3.8\%$), the two parameters increase dramatically; that is, the increasing production of C_1 and C_2 , which is a typical oil secondary cracking though the contribution of kerogen primary cracking, cannot be excluded.⁷⁰ The critical temperatures of C_5 , C_4 , C_3 , and C_2 occur in this stage (Figure 5), suggesting that decomposition rates exceed generation rates for C_5 , C_4 , C_3 , and C_2 , in turn, which is another evidence for oil secondary cracking. Stage 4: finally (easy $R_o = 3.8–4.5\%$), $\ln C_1/C_2$ continues to increase, and $\ln C_2/C_3$ is almost stable when the temperature is above 548 °C, which can be attributed to the gas cracking at high pyrolysis temperatures, especially C_{2-3} into C_{2-1} .

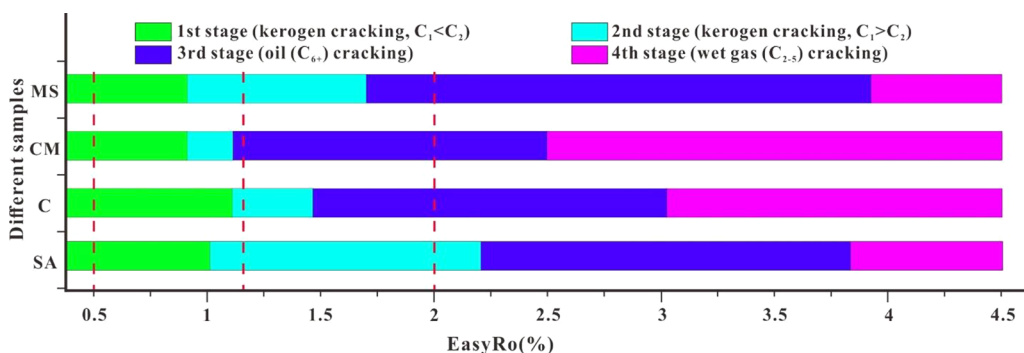


Figure 11. Plot of the stages of gas evolution (source) in different maturity stages of source rocks of different lithologies. MS is short for marine shale (data from Wang et al.⁶⁵); CM is short for coal measure mudstone; C is short for coal (data from Zhao et al.⁴⁵); SA is short for saline lacustrine shale (this study). Those samples are used for the similar closed gold tube thermal simulation experiments.

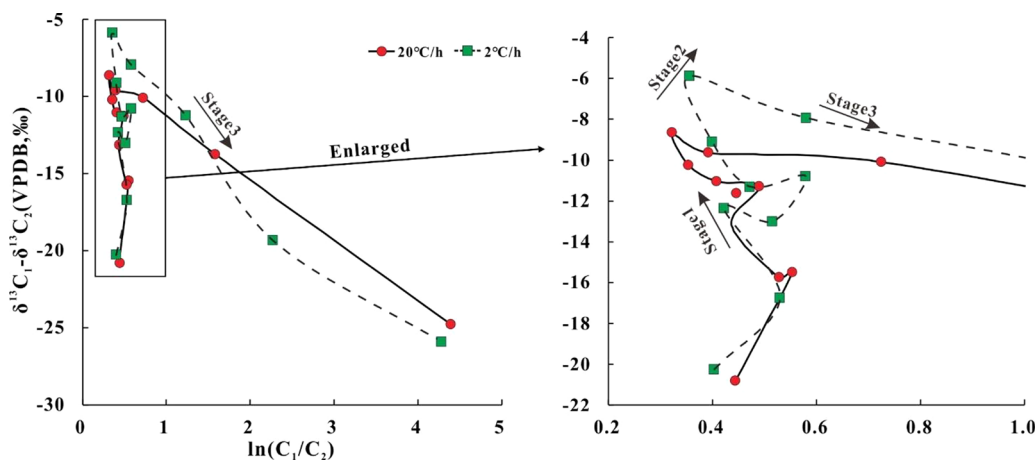


Figure 12. Plot of $\delta^{13}\text{C}_1 - \delta^{13}\text{C}_2$ versus $\ln C_1/C_2$ for gases generated from the SA shale at the heating rates of 20 and 20 °C/h in the closed gold tube thermal simulation experiments showing the process of gas evolution. SA represents the saline area of the Dongpu Depression.

5.2.1.2. NA Sample. Stage 1: when the temperature is between 299.3 and 319.4 °C (easy $R_o = 0.56\text{--}0.65\%$), the trend is similar to stage 1 of the SA sample. Stage 2: at 319.4–379.5 °C (easy $R_o = 0.65\text{--}1.04\%$), this interval is significantly different from stage 2 of the SA sample. The value of $\ln C_1/C_2$ decreases from 1.21 to 0.69, and the value of $\ln C_2/C_3$ increases from 0.15 to 0.87, which indicates that the trend of gas generation in this interval is prone to generate C_2 , followed by C_1 and then C_3 . Stages 3 and 4: when the temperature is between 379.5 and 524.2 °C (easy $R_o = 1.04\text{--}3.38\%$) and between 524.2 and 599.7 °C (easy $R_o = 3.38\text{--}4.45\%$), the two stages are both similar to stages 3 and 4 of the SA sample; therefore, they are not demonstrated again.

Actually, many researchers have conducted the confined gold cube thermal simulation experiments on different types of samples, including the coal (C), coal measure mudstone (CM),⁴⁹ and marine shale (MS).⁷³ Almost all scholars divide the process of gas evolution into four stages using the plot of $\ln(C_1/C_2)$ versus $\ln(C_2/C_3)$. However, there is a significant difference in the easy R_o (temperature) range of each stage in several studies, although the specific reactions are similar, including this experiment on saline rifting lacustrine shale (SA). As shown in Figure 11 and Table 3, the gas evolution process of SA is similar to MS and differs from that of C and CM. It can be concluded that the origins of hydrocarbon gases in shale (I or II kerogen) and coal (III kerogen) are different in different maturity stages. More specifically, in the mature stage, the origins of gases in different samples are similar and mainly

kerogen cracking. In the high-mature stage, the gas generated from the shale (SA and MS) comes from kerogen cracking, followed by oil cracking, and that from the coal (C and CM) mainly comes from oil cracking. In the overmature stage, the process of oil cracking into gas lasts to a longer easy R_o in shale than that in coal and wet gas cracking is a main way for all samples to generate slighter gases.

5.2.2. $\delta^{13}\text{C}_1 - \delta^{13}\text{C}_2$ versus $\ln C_1/C_2$. The plot of $\delta^{13}\text{C}_1 - \delta^{13}\text{C}_2$ versus $\ln C_1/C_2$ proposed by Prinzhofer and Huc⁷⁰ has been used in distinguishing gases from kerogen or oil cracking in previous studies.^{49,56,59,71,73} Generally, with an increasing temperature, the difference in the isotopic ratios decreases toward zero but remains negative in a typical fractionation associated with thermogenic gases.⁷⁰ Because of the lack of valid data, the analysis for the NA sample of $\delta^{13}\text{C}_1 - \delta^{13}\text{C}_2$ versus $\ln C_1/C_2$ is not conducted. As shown in Figure 12, the curves at two heating rates can be divided into three similar stages; therefore, the trend at the heating rate of 2 °C/h is used as an example. (1) At the initial stage, with the increase of the temperature, the value of $\ln C_1/C_2$ decreases slightly and $\delta^{13}\text{C}_1 - \delta^{13}\text{C}_2$ increases substantially, which can be attributed to the preferential generation of kerogen cracking into C_2 over C_1 . (2) At the second stage of the whole reaction, the two parameters show a modest upward trend, which indicates that C_1 has the top prior to being generated in comparison to C_2 . Moreover, the absolute value of $\delta^{13}\text{C}_1 - \delta^{13}\text{C}_2$ increases to the maximum, which suggests that the difference between $\delta^{13}\text{C}_1$ and $\delta^{13}\text{C}_2$ decreases to the minimum. (3) There is a rapid

growth in $\ln C_1/C_2$ and a significant decrease in $\delta^{13}C_1 - \delta^{13}C_2$ at the final stage. As shown in section 4.2.2, the C_{1-5} yield tends to be stable and the C_{2-5} yield decreases substantially in this temperature range. In contrast, the CH_4 yield continues to increase. This indicates that the source of CH_4 is mainly the cracking of C_{2-5} . Generally, the difference between $\delta^{13}C_1$ and $\delta^{13}C_2$ enlarges in the process of wet gas (C_{2-5}) cracking.⁵⁹

5.3. Extrapolation to Geological Conditions. The kinetic parameters (activation energy and frequency factor) obtained from the closed gold tube thermal simulation experiment can be used to reconstruct the history of hydrocarbon generation in the geological period.^{30,53,61–64} The paleo-geothermal parameters and basic geological data of SA and NA in the Dongpu Depression have been studied deeply.⁴⁸ The evolution of the geothermal gradient in different sub-depressions of the Dongpu Depression is similar. When the results of Liu and Ren are taken as an example, the geothermal gradient evolution curve is bimodal and the two peaks are distributed in the late stage of Es_3 and the middle and late stages of Ed .⁴⁸ This geothermal trend is agreeable with tectonic evolution. In the Paleogene, the Dongpu Depression has experienced the initial faulting stage in Es_4 , the intense faulting stage in Es_3 , and the depressed stage during the period from Es_2 to Ed .⁷⁵ Therefore, in the period of Es_3 , mantle uplift and crust thinning or splitting are caused by intense rifting and then deep heat carriers (magma and hydrothermal fluid) flow up to the shallow part of the crust or spill out to the surface through the deep and large faults, resulting in a higher geothermal background. The short-term tectonic uplift resulted in the decrease of the geothermal gradient from the late stage of Es_3 to the early stage of Es_2 . Subsequently, the late rifting increased the mantle heat flow, causing the geothermal gradient to increase again.⁷⁵

On the basis of the experimental geochemical data and hydrocarbon generation kinetic data in this study, combined with the thermal history data and geological and massive geochemical data of SA and NA studied by previous researchers, the gas generation history of SA and NA is conducted.⁷⁶ As shown in Figure 13a, the SA shale and NA mudstone began to generate gases 40 Ma. This is consistent with the fact that Es_4 and Es_3 source rocks have just entered the mature stage ($R_o > 0.5\%$) at this time when the Dongpu Depression was experiencing the intense faulting stage. It can be assumed that the conversion ratio range of 20–80% can represent the main hydrocarbon generation stage, in which 20 and 80% are the lower and upper limits of this stage, respectively.⁷⁷ The main gas generation stage of SA and NA is 34–25 and 33–24 Ma, respectively, which is the late Es_1 and Ed periods in geologic history (Figure 13b). This main hydrocarbon generation stage is in the depression stage of the Dongpu Depression with the deepest depth and the largest subsidence amplitude. After that, the Dongpu Depression rose gradually, which results in the destination of gas generation.

6. CONCLUSION

(1) The results of geochemical data and oil yields from thermal simulation experiments show that, in comparison to NA samples, SA samples are fairly good oil-prone source rocks. The integrated analysis of source rocks in some SLRBs (Dongpu Depression, Dongying Depression, Qianjiang Depression, and Qaidam Basin) further verify the oil-prone property. However, the gas yields indicate that the shale in SA has the potential of gas generation, which can provide a

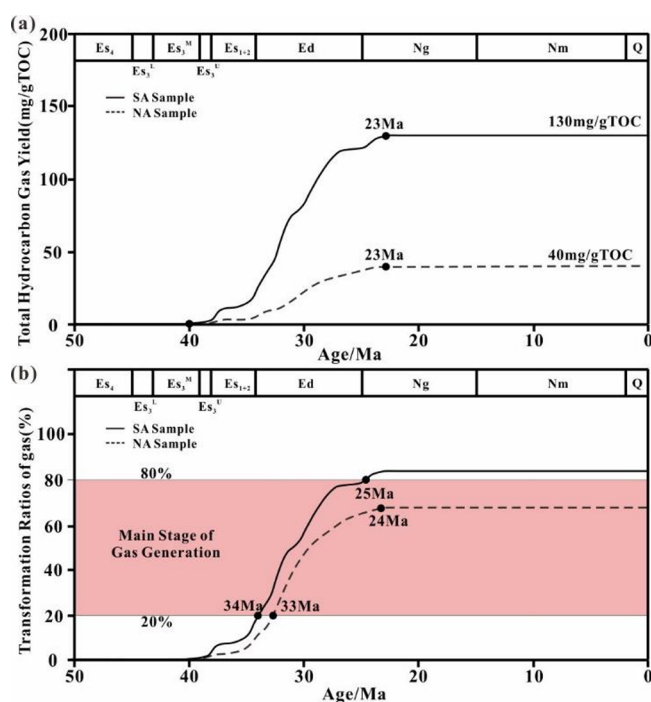


Figure 13. Gas generation history for SA and NA of the Dongpu Depression under geological conditions: (a) total gas (C_{1-5}) yield under geological conditions and (b) transformation ratio of (C_{1-5}). The lower and upper limits of the main gas generation stage are from Wang et al.⁶⁹ SA and NA represent the saline area and non-saline area of the Dongpu Depression, respectively.

hydrocarbon source for shale gas reservoirs. (2) According to $\ln C_2/C_3$, $\ln C_1/C_2$, $\delta^{13}C_1 - \delta^{13}C_2$, and hydrocarbon yields, the process of gas generation for SA and NA can be divided into three stages: (1) kerogen cracking into gas (easy $R_o = 0.6$ – 2.2%), (2) oil cracking into gas (easy $R_o = 2.2$ – 3.8%), and (3) wet gas cracking into lighter gas (easy $R_o = 3.8$ – 4.5%). Moreover, in comparison to other types of samples (marine shale, coal, and coal mudstone), the SA sample can generate gas mainly by kerogen cracking in the high-mature stage and oil cracking in the overmature stage. (3) The kinetic parameters of gas are applied in the practical geological conditions, and the results show that the SA and NA samples start to generate gas in 40 Ma, and the final gas yield for SA and NA samples is 130 and 40 mg/g of TOC, respectively. The main gas generation stage of SA and NA samples is in 34–25 and 33–24 Ma, respectively, which is in the depression stage of the Dongpu Depression with the deepest depth and the largest subsidence amplitude.

■ AUTHOR INFORMATION

Corresponding Author

Fujie Jiang – State Key Laboratory of Petroleum Resources and Prospecting, China University of Petroleum (Beijing), Beijing 102249, People's Republic of China; orcid.org/0000-0002-0089-2972; Phone: +86-13811148227; Email: fjhtb@163.com

Authors

Pengyuan Zhang – State Key Laboratory of Petroleum Resources and Prospecting, China University of Petroleum (Beijing), Beijing 102249, People's Republic of China; Key Laboratory of Cenozoic Geology and Environment, Institute

of Geology and Geophysics, Chinese Academy of Sciences, Beijing 100029, People's Republic of China

Chenxi Zhu – State Key Laboratory of Petroleum Resources and Prospecting, China University of Petroleum (Beijing), Beijing 102249, People's Republic of China

Renda Huang – State Key Laboratory of Petroleum Resources and Prospecting, China University of Petroleum (Beijing), Beijing 102249, People's Republic of China

Tao Hu – State Key Laboratory of Petroleum Resources and Prospecting, China University of Petroleum (Beijing), Beijing 102249, People's Republic of China; orcid.org/0000-0002-0578-4364

Tianwu Xu – Zhongyuan Oilfield Branch, SINOPEC, Puyang, Henan 457001, People's Republic of China

Wendu Li – State Key Laboratory of Petroleum Resources and Prospecting, China University of Petroleum (Beijing), Beijing 102249, People's Republic of China

Hang Xiong – State Key Laboratory of Petroleum Resources and Prospecting, China University of Petroleum (Beijing), Beijing 102249, People's Republic of China

Complete contact information is available at:

<https://pubs.acs.org/10.1021/acs.energyfuels.0c03965>

Notes

The authors declare no competing financial interest.

ACKNOWLEDGMENTS

This work was supported by the “Periodical Changes of Salinity in the Lake Water and Mechanism of Different Organic Matter Enrichment in the Saline Lacustrine Basins” from SINOPEC Petroleum Exploration and Production Research Institute and the National Natural Science Foundation of China (Grant 41872128). The authors sincerely thank the Research Institute of Exploration and Development, Zhongyuan Oilfield, SINOPEC, for the core samples and data of basic geological setting.

NOMENCLATURE

SLRB = saline lacustrine rifting basin

BBB = Bohai Bay Basin

OM = organic matter

SA = saline area of the Dongpu Depression

NA = non-saline area of the Dongpu Depression

Es₄ = fourth member of the Shahejie Formation

Es₃ = third member of the Shahejie Formation

Es₂ = second member of the Shahejie Formation

Es₁ = first member of the Shahejie Formation

Ng = Guantao Formation

Nm = Minghuazhen Formation

Qp = Pingyuan Formation

TOC = total organic carbon

T_{max} = peak temperature of pyrolysis

R_o = vitrinite reflectance

HI = hydrogen index

C = gas transformation ratio

A = frequency factor value

REFERENCES

(1) Zou, C. N.; Yang, Z.; Tao, S. Z.; Yuan, X. J.; Zhu, R.; Hou, L. H.; Wu, S. T.; Sun, L.; Zhang, G. S.; Bai, B.; Wang, L.; Gao, X. H.; Pang, Z. L. Continuous hydrocarbon accumulation over a large area as a distinguishing characteristic of unconventional petroleum: The Ordos Basin; North–Central China. *Earth-Sci. Rev.* **2013**, *126*, 358–369.

(2) Schmoker, J. W. Method for assessing continuous—Type (unconventional) hydrocarbon accumulations. In *National Assessment of United States Oil and Gas Resources—Results, Methodology, and Supporting Data*; Gautier, D. L., Dolton, G. L., Takahashi, K. I., Varnes, K. L., Eds.; U.S. Geological Survey: Reston, VA, 1995; U.S. Geological Survey Digital Data Series DDS-30.

(3) Klemme, H. D.; Ulmishek, G. F. Effective petroleum source rocks of the world: Stratigraphic distribution and controlling depositional factors. *AAPG Bull.* **1991**, *75* (12), 1809–1851.

(4) Dyman, T. S.; Crovelli, R. A.; Bartberger, C. E.; Takahashi, K. I. Worldwide estimates of deep natural gas resources based on the US Geological Survey World Petroleum Assessment 2000. *Nat. Resour. Res.* **2002**, *11*, 207–218.

(5) Wei, J. Y.; Wang, Y. L.; Wang, G.; Wei, Z. F.; He, W. Geochemistry and shale gas potential of the lower Permian marine-continental transitional shales in the Eastern Ordos Basin. *Energy Explor. Exploit.* **2020**, No. 11, 014459872097924.

(6) Zou, C. N.; Zhang, G. S.; Yang, Z.; Tao, S. Z.; Hou, L. H.; Zhu, R. K.; Yuan, X. J.; Ran, Z. Q.; Li, D. H.; Wang, Z. P. Geological concepts, characteristics, resource potential and key techniques of unconventional hydrocarbon: On unconventional petroleum geology. *Pet. Explor. Dev.* **2013**, *40* (4), 413–428.

(7) Sharma, S.; Agrawal, V.; Akondi, R. N. Role of biogeochemistry in efficient shale oil and gas production. *Fuel* **2020**, *259*, 116207.

(8) Sun, L. D.; Zou, C. N.; Zhu, R. K.; Zhang, Y. H.; Zhang, S. C.; Zhang, B. M.; Zhu, G. Y.; Gao, Z. Y. Formation, distribution and potential of deep hydrocarbon resources in China. *Pet. Explor. Dev.* **2013**, *40* (6), 687–695.

(9) Jiang, C.; Lu, T.; Zhang, D.; Li, G.; Duan, M.; Chen, Y.; Liu, C. An experimental study of deformation and fracture characteristics of shale with pore–water pressure and under triaxial cyclic loading. *R. Soc. Open Sci.* **2018**, *5*, 180670.

(10) Rasouli, V. Geomechanics of gas shales. In *Fundamentals of Gas Shale Reservoirs*; Rezaee, R., Ed.; John Wiley & Sons, Inc.: Hoboken, NJ, 2015; Chapter 8, pp 169–190, DOI: 10.1002/9781119039228.ch8.

(11) U.S. Energy Information Administration (EIA). *International Energy Outlook 2013*; EIA: Washington, D.C., 2013.

(12) Zou, C.; Yang, Z.; He, D.; Wei, Y.; Li, J.; Jia, A.; Chen, J.; Zhao, Q.; Li, Y.; Li, J.; Yang, S. Theory, technology and prospects of conventional and unconventional natural gas. *Pet. Explor. Dev.* **2018**, *45* (4), 604–618.

(13) Zou, C. N.; Yang, Z.; He, D. B.; Wei, Y. S.; Li, J.; Jia, A. L.; Chen, J. J.; Zhao, Q.; Li, Y. L.; Li, J.; Yang, S. Theory; technology and prospects of conventional and unconventional natural gas. *Pet. Explor. Dev.* **2018**, *45* (4), 604–618.

(14) Zou, C. N.; Guo, J. L.; Jia, A. L.; Wei, Y. S.; Yan, H. J.; Jia, C. Y.; Tang, H. F. Connotations of scientific development of giant gas fields in China. *Nat. Gas Ind. B* **2020**, *7* (5), 533–546.

(15) Kembal-Cook, S.; Bar-Ilan, A.; Grant, J.; Parker, L.; Jung, J.; Santamaria, W.; Mathews, J.; Yarwood, G. Ozone Impacts of Natural Gas Development in the Haynesville Shale. *Environ. Sci. Technol.* **2010**, *44* (24), 9357–9363.

(16) Wang, Q.; Zhou, W.; Hu, Q. H.; Xu, H.; Meendsen, F.; Shu, Y.; Qiao, H. G. Pore Geometry Characteristics and Fluid–Rock Interaction in the Haynesville Shale, East Texas, United States. *Energy Fuels* **2021**, *35* (1), 237–250.

(17) Cesar, J.; Becker, V.; Mayer, B. Organic and isotope geochemistry analysis of petroleum condensates from the unconventional portion of the Montney Formation, Western Canada. *Fuel* **2020**, *282*, 118879.

(18) Wei, Z. F.; Wang, Y. L.; Wang, G.; Zhang, T.; He, W.; Ma, X. Y. Reconstructing the Climatic–Oceanic Environment and Exploring the Enrichment Mechanism of Organic Matter in the Black Shale across the Late Ordovician–Early Silurian Transition on the Upper Yangtze Platform Using Geochemical Proxies. *Omega*. **2020**, *5* (42), 27442–27454.

- (19) Tissot, B. P.; Welte, D. H. *Petroleum Formation and Occurrence*; Springer-Verlag: Berlin, Germany, 1984; DOI: 10.1007/978-3-642-87813-8.
- (20) Xue, Y. A. The breakthrough of the deep-buried gas exploration in the Bohai Sea area and its enlightenment. *Nat. Gas Ind.* **2019**, *39* (1), 11–20 (in Chinese with an English abstract).
- (21) Mello, U. T.; Karner, G. D. Development of sediment overpressure and its effective thermal maturation: Application to the Gulf of Mexico Basin. *AAPG Bull.* **1996**, *80* (9), 1367–1396.
- (22) Li, W.; Cao, J.; Shi, C.; Xu, T.; Zhang, H.; Zhang, Y. Shale oil in saline lacustrine systems: A perspective of complex lithologies of fine-grained rocks. *Mar. Pet. Geol.* **2020**, *116*, 104351.
- (23) Hu, T.; Pang, X. Q.; Jiang, S.; Wang, Q. F.; Zheng, X. W.; Ding, X. G.; Zhao, Y.; Zhu, C. X.; Li, H. Oil content evaluation of lacustrine organic-rich shale with strong heterogeneity: A case study of the Middle Permian Lucaogou Formation in Jimusaer Sag, Junggar Basin, NW China. *Fuel* **2018**, *221*, 196–205.
- (24) Jiang, F. J.; Wang, Q. F.; Liu, L. F.; Gao, X.; Hu, T. Geological and geochemical characteristics of the Middle–Lower Jurassic shales in the Kuqa Depression, Tarim Basin, an evaluation of shale gas resources. *Aust. J. Earth Sci.* **2018**, *65* (4), 557–573.
- (25) Jiang, F.; Chen, D.; Chen, J.; Li, Q.; Liu, Y.; Shao, X.; Hu, T.; Dai, J. Fractal Analysis of Shale Pore Structure of Continental Gas Shale Reservoir in the Ordos Basin, NW China. *Energy Fuels* **2016**, *30* (6), 4676–4689.
- (26) Jiang, F. J.; Chen, D.; Wang, Z. F.; Xu, Z. Y.; Chen, J.; Liu, L.; Huyan, Y. Y.; Liu, Y. Pore characteristic analysis of a lacustrine shale: A case study in the Ordos Basin, NW China. *Mar. Pet. Geol.* **2016**, *73*, 554–571.
- (27) Hu, T.; Pang, X.; Jiang, S.; Wang, Q.; Xu, T.; Lu, K.; Huang, C.; Chen, Y.; Zheng, X. Impact of Paleosalinity, Dilution, Redox, and Paleoproductivity on Organic Matter Enrichment in a Saline Lacustrine Rift Basin: A Case Study of Paleogene Organic-Rich Shale in Dongpu Depression, Bohai Bay Basin, Eastern China. *Energy Fuels* **2018**, *32* (4), 5045–5061.
- (28) Shao, X. H.; Pang, X. Q.; Li, H.; Hu, T.; Xu, T. W.; Xu, Y.; Li, B. Y. Pore network characteristics of lacustrine shales in the Dongpu Depression, Bohai Bay Basin, China, with implications for oil retention. *Mar. Pet. Geol.* **2018**, *96*, 457–473.
- (29) Sweeney, J. J.; Burnham, A. K. Evaluation of a simple model of vitrinite reflectance based on chemical kinetics. *AAPG Bull.* **1990**, *74*, 1559–1570.
- (30) Behar, F.; Vandenbroucke, M.; Tang, Y.; Marquis, F.; Espitalié, J. Thermal cracking of kerogen in open and closed system: Determination of kinetic parameters and stoichiometric coefficients for oil and gas generation. *Org. Geochem.* **1997**, *26*, 321–339.
- (31) Seewald, J. S.; Benitez-Nelson, B. C.; Whelan, J. K. Laboratory and theoretical constraints on the generation and composition of natural gas. *Geochim. Cosmochim. Acta* **1998**, *62*, 1599–1617.
- (32) Hill, R. J.; Tang, Y.; Kaplan, I. R. Insights into oil cracking based on laboratory experiments. *Org. Geochem.* **2003**, *34*, 1651–1672.
- (33) Behar, F.; Lorant, F.; Lewan, M. D. Role of NSO compounds during primary cracking of a Type II kerogen and a Type III lignite. *Org. Geochem.* **2008**, *39*, 1–22.
- (34) Behar, F.; Roy, S.; Jarvie, D. Artificial maturation of a Type I kerogen in closed system: Mass balance and kinetic modeling. *Org. Geochem.* **2010**, *41*, 1235–1247.
- (35) Mi, J. K.; Zhang, S. C.; Wang, X. M. Comparison of different hydrocarbon generation simulation approaches and key technique. *Pet. Geol. Exp.* **2009**, *31* (4), 409–414 (in Chinese with an English abstract).
- (36) Qi, J. F.; Zhang, Y. W.; Lu, K. Z.; Yang, J. Cenozoic tectonic evolution in Bohai Bay Basin province. *J. Chin. Univ. Pet.* **1995**, *19*, 1–6 (in Chinese with an English abstract).
- (37) Jiang, Y. L.; Liu, P.; Liu, H.; Song, G. Q.; Wang, Y. S.; Cui, X. J. Difference of reservoir forming conditions of different depressions and accumulation models of Neogene hydrocarbon in Bohai Bay Basin. *J. Chin. Univ. Pet.* **2014**, *38* (1), 14–21 (in Chinese with an English abstract).
- (38) Wang, Q. F.; Jiang, F. J.; Ji, H. C.; Jiang, S.; Liu, X. H.; Zhao, Z.; Wu, Y. Q.; Xiong, H.; Li, Y.; Wang, Z. Effects of paleosedimentary environment on organic matter enrichment in a saline lacustrine rift basin—A case study of Paleogene source rock in the Dongpu Depression, Bohai Bay Basin. *J. Pet. Sci. Eng.* **2020**, *195*, 107658.
- (39) Qi, X. Y.; Huang, X. X.; Shou, J. F.; Li, Y. Y. The relation of salt deposits to oil and gas accumulation in Dongpu Depression. *Acta Pet. Sin.* **1992**, *13* (1), 23–29 (in Chinese with an English abstract).
- (40) He, X. L.; Wang, X. L.; Wu, X. L.; Wang, Y. S.; Jiang, Y. J. Genesis Type of Natural Gas in Dongpu Depression and Its Range of Profitability of Exploration. *Fault-Block Oil Gas Field* **2002**, *9* (6), 25–28 (in Chinese with an English abstract).
- (41) Chen, S. P.; Qi, J. F.; Wang, D. R.; Cheng, X. K.; Zhao, Y. B.; Xu, Z. Q.; Xie, Q.; Sun, H. L. Fault systems and transfer structures in Dongpu Sag. *Acta Pet. Sin.* **2007**, *28* (1), 43–49 (in Chinese with an English abstract).
- (42) Cheng, X. S.; Qi, J. F.; Chen, S. P.; Wang, F. Y.; Gu, Q.; Liu, L. L. Discussion on structural units of Dongpu Depression. *Fault-Block Oil Gas Field* **2009**, *16* (4), 15–18 (in Chinese with an English abstract).
- (43) Su, H.; Qu, L. P.; Li, G. X.; Wang, Y. J.; Song, J. Balanced section and tectonic evolution in the Dongpu Depression. *Geophys. Prospect. Pet.* **2000**, *35* (4), 469–478 (in Chinese with an English abstract).
- (44) Tang, L. J.; Wang, G. M.; Zhou, X. H.; Jin, W. Z.; Yu, Y. X. Cenozoic geotectonic evolution of the Bohai Basin. *Geol. J. Chin. Univ.* **2008**, *14* (2), 191–198 (in Chinese with an English abstract).
- (45) Wu, D. S.; Guo, J. H.; Wu, Z. Y.; He, H. Discussion on the bottom boundary and stratigraphic composition of the southwest depression of Dongpu Depression. *Pet. Explor. Dev.* **1998**, *25* (4), 26–28 (in Chinese).
- (46) Tang, L.; Song, Y.; Pang, X. Q.; Jiang, Z. X.; Guo, Y. C.; Zhang, H. A.; Pan, Z. H.; Jiang, H. Effects of paleo sedimentary environment in a saline lacustrine basin on organic matter accumulation and preservation—A case study from the Dongpu Depression, Bohai Bay Basin, China. *J. Pet. Sci. Eng.* **2020**, *185*, 106669.
- (47) Chen, J.; Lu, K.; Feng, Y.; Yuan, K. H.; Wang, D. B.; Cui, H.; Zhang, W. J. Evaluation on hydrocarbon source rocks in different environments and characteristics of hydrocarbon generation and expulsion in Dongpu Depression. *Fault-Block Oil Gas Field* **2012**, *19* (1), 35–38 (in Chinese with an English abstract).
- (48) Liu, L.; Ren, Z. L. Thermal evolution of Dongpu Sag. *Pet. Explor. Dev.* **2007**, *34* (4), 419–423.
- (49) Zhao, Z. F.; Pang, X. Q.; Jiang, F. J.; Wang, K.; Li, L. L.; Zhang, K.; Zheng, X. W. Hydrocarbon generation from confined pyrolysis of lower Permian Shanxi Formation coal and coal measure mudstone in the Shenfu area, northeastern Ordos Basin, China. *Mar. Pet. Geol.* **2018**, *97*, 355–369.
- (50) Lu, X. S.; Jiang, Y. L.; Chang, Z. H.; Wu, X. L. Calculation of the Erosion Thickness of Dongying Formation in Dongpu Depression and Its Significance. *Bull. Geol. Sci. Technol.* **2007**, *26* (2), 8–12 (in Chinese with an English abstract).
- (51) Jin, G. X.; Wei, L. H.; Zhang, D. X. The Analyses of Reservoir Forming Process in Dongpu Depression. *Inn. Mong. Petrochem. Ind.* **2010**, *11*, 55–56 (in Chinese with an English abstract).
- (52) Jasper, K.; Krooss, B. M.; Flajs, G.; Hartkopf-Fröder, C.; Littke, R. Characteristics of type III kerogen in coal-bearing strata from the Pennsylvanian (Upper Carboniferous) in the Ruhr Basin, Western Germany: Comparison of coals, dispersed organic matter, kerogen concentrates and coal–mineral mixtures. *Int. J. Coal Geol.* **2009**, *80*, 1–19.
- (53) Liu, J. Z.; Tang, Y. C. A case study of prediction of methane production by kinetic method of kerogen hydrocarbon generation. *Chin. Sci. Bull.* **1998**, *10*, 1187–1191 (in Chinese).
- (54) Mao, R.; Mi, J. K.; Zhang, S. C.; He, K. Study on the hydrocarbon generation characteristics of different coaly source rocks

by gold–tube pyrolysis experiments. *Nat. Gas Geosci.* **2012**, *23*, 1127–1134 (in Chinese with an English abstract).

(55) Ning, K. C. Comparison of Characteristics of Salt-Bearing and Salt-Free Source Rock of Dongpu Depression. Master's Thesis, China University of Petroleum (Beijing), Beijing, China, 2017; pp 52–53, 63 (in Chinese with an English abstract).

(56) Lorant, F.; Prinzhofer, A.; Behar, F.; Huc, A. Y. Carbon isotopic and molecular constraints on the formation and the expulsion of thermogenic hydrocarbon gases. *Chem. Geol.* **1998**, *147*, 249–264.

(57) Tian, H.; Xiao, X. M.; Wilkins, R. W. T.; Li, X. Q.; Gan, H. J. Gas sources of the YN2 gas pool in the Tarim Basin – evidence from gas generation and methane carbon isotope fractionation kinetics of source rocks and crude oils. *Mar. Pet. Geol.* **2007**, *24*, 29–41.

(58) Peng, W. L.; Hu, G. Y.; Liu, Q. Y.; Jia, N.; Fang, Z. S.; Gong, D. Y.; Yu, C.; Lv, Y.; Wang, P. W.; Feng, Z. Q. Research status on thermal simulation experiment and several issues for concerns. *Nat. Gas Geosci.* **2018**, *29* (9), 1252–1263 (in Chinese with an English abstract).

(59) Wang, Z.; Wang, Y.; Wu, B.; Wang, G.; Sun, Z.; Xu, L.; Zhu, S.; Sun, L.; Wei, Z. Hydrocarbon gas generation from pyrolysis of extracts and residues of low maturity solid bitumens from the Sichuan Basin, China. *Org. Geochem.* **2017**, *103*, 51–62.

(60) Wang, T. S.; Geng, A. S.; Li, X.; Xu, Z. H. Gas-generation mechanism of the pyrolysis of asphaltenes in marine crude oil and its geological application. *Acta Sedimentol. Sin.* **2010**, *28*, 808–814.

(61) Tissot, B. P.; Pelet, R.; Ungerer, P. Thermal history of sedimentary basins, maturation indices, and kinetics of oil and gas generation. *AAPG Bull.* **1987**, *71*, 1445–1466.

(62) Ungerer, P.; Pelet, R. Extrapolation of the kinetics of oil and gas formation from laboratory experiments to sedimentary basins. *Nature* **1987**, *327*, 52–54.

(63) Braun, R. L.; Burnham, A. K. Analysis of chemical reaction kinetics using a distribution of activation energies and simpler models. *Energy Fuels* **1987**, *1*, 153–161.

(64) Behar, F.; Kressmann, S.; Rudkiewicz, J. L.; Vandenbroucke, M. Experimental simulation in a confined system and kinetic modeling of kerogen and oil cracking. *Org. Geochem.* **1992**, *19*, 173–189.

(65) Liu, G. D. *Petroleum Geology*; Petroleum Industry Press: Beijing, China, 2009; pp 157–161.

(66) Zhu, G. Y.; Jin, Q.; Dai, J. X.; Zhang, S. C.; Zhang, L. Y.; Li, J. Investigation on salt lake source rocks for Middle Shazi Column of Dongying Depression. *Geol. J. China Univ.* **2004**, *10* (2), 257–266 (in Chinese with an English abstract).

(67) Li, L.; Wang, Z. X.; Zheng, Y. H.; Chen, F. L.; Wu, S. Q.; Qi, Z. X.; Liu, A. W. Mechanism of shale oil enrichment from the salt cyclotherm in Qian3 Member of Qianjiang sag, Jiangnan basin. *Earth Sci.* **2019**, *44* (3), 1012–1023 (in Chinese with an English abstract).

(68) Zhang, B.; He, Y. Y.; Chen, Y.; Meng, Q. Y.; Yuan, L. Geochemical characteristics and oil accumulation significance of the high-quality saline lacustrine source rocks in the western Qaidam Basin, NW China. *Acta Pet. Sin.* **2017**, *38* (10), 1158–1167. (in Chinese with an English abstract)

(69) Ricchiuto, T.; Schoell, M. Origin of natural gases in the Apulian Basin in south Italy: A case history of mixing of gases of deep and shallow origin. *Org. Geochem.* **1988**, *13*, 311–318.

(70) Prinzhofer, A. A.; Huc, A. Y. Genetic and post–genetic molecular and isotopic fractionations in natural gases. *Chem. Geol.* **1995**, *126* (95), 281–290.

(71) Hill, R. J.; Tang, Y. C.; Kaplan, I. R. Insights into oil cracking based on laboratory experiments. *Org. Geochem.* **2003**, *34*, 1651–1672.

(72) Tian, H.; Xiao, X. M.; Wilkins, R. W. T.; Gan, H. J.; Guo, L. G.; Yang, L. G. Genetic origins of marine gases in the Tazhong area of the Tarim basin, NW China: Implications from the pyrolysis of marine kerogens and crude oil. *Int. J. Coal Geol.* **2010**, *82*, 17–26.

(73) Wang, Q. T.; Lu, H.; Greenwood, P.; Shen, C. C.; Liu, J. Z.; Peng, P. A. Gas evolution during kerogen pyrolysis of Estonian Kukersite shale in confined gold tube system. *Org. Geochem.* **2013**, *65*, 74–82.

(74) Zhao, W. Z.; Wang, Z. Y.; Zhang, S. C.; Wang, H. J.; Wang, Y. P. Oil cracking: An important way for highly efficient generation of gas from marine source rock kitchen. *Chin. Sci. Bull.* **2005**, *50*, 2628–2635.

(75) Su, H.; Qu, L. P.; Zhang, J. C.; Wang, P. X.; He, F.; Wang, M. Tectonic evolution and extensional pattern of rifted basin: A case study of Dongpu Depression. *Oil Gas Geol.* **2006**, *27* (1), 70–77 (in Chinese with an English abstract).

(76) Li, L.; Zuo, Y. H.; Tang, S. H.; Zhang, S. H. The Cenozoic thermal history in the Dongpu sag; Bohai Bay Basin. *Geol. Explor.* **2017**, *52* (3), 594–600.

(77) Wang, Q.; Zou, H. Y.; Hao, F.; Zhu, Y. M.; Zhou, X. H.; Wang, Y. B.; Tian, J. Q.; Liu, J. Z. Modeling hydrocarbon generation from the Paleogene source rocks in Liaodong Bay, Bohai Sea: A study on gas potential of oil–prone source rocks. *Org. Geochem.* **2014**, *76*, 204–219.